SAO participation in the GOME and SCIAMACHY Satellite Instrument Programs

NASA Grant NAG5-11677

Annual Report No. 2

For the period 1 July 2003 through 30 November 2004

Principal Investigator
Dr. Kelly Chance

December 2004

Prepared for

National Aeronautics and Space Administration
Washington, DC 20546

SMITHSONIAN INSTITUTION
ASTROPHYSICAL OBSERVATORY
CAMBRIDGE, MASSACHUSETTS 02138

Director: Charles Alcock

The Smithsonian Astrophysical Observatory
is a member of the
Harvard-Smithsonian
Center for Astrophysics

The NASA Technical Officer for this Grant is Ernest Hilsenrath,
Code 916.0, NASA Goddard Space Flight Center.

SAO Participation in the GOME and SCIAMACHY Satellite Instrument Programs

NASA Grant NAG5-11677

Progress as of November 30, 2004

Principal Investigator
Dr. Kelly Chance

Co-Investigator
Dr. Thomas Kurosu

1. Introduction

This report summarizes the progress on our three-year program of research to refine the measurement capability for satellite-based instruments that monitor ozone and other trace species in the Earth's stratosphere and troposphere, to retrieve global distributions of these and other constituents from the GOME and SCIAMACHY satellite instruments, and to conduct scientific studies for the ILAS instruments. This continues our involvements as a U.S. participant in GOME and SCIAMACHY since their inception, and as a member of the ILAS-II Science Team. These programs have led to the launch of the first satellite instrument specifically designed to measure height-resolved ozone, including the tropospheric component (GOME), and the development of the first satellite instrument that will measure tropospheric ozone simultaneously with NO_2, CO, HCHO, N_2O, H_2O, and CH_4 (SCIAMACHY). The GOME program now includes the GOME-2 instruments, to be launched on the Eumetsat Metop satellites, providing long-term continuity in European measurements of global ozone that complement the measurements of the TOMS, SBUV, OMI, OMPS instruments.

The research primarily focuses on two areas: *Data analysis*, including algorithm development and validation studies that will improve the quality of retrieved data products, in support for future field campaigns (to complement in situ and airborne campaigns with satellite measurements), and *scientific analyses* to be interfaced to atmospheric modeling studies.

2. Progress in Second Year of Studies

2.1 SCIAMACHY

The SCIAMACHY instrument was launched on the Envisat satellite on March 1, 2002. At present, SCIAMACHY is still in the process of validation. We have been working with the European Space Agency, through the SCIAMACHY Algorithm Development and Data Usage subgroup (SADDU) of the SCIAMACHY Science Advisory Group

(SSAG), and the German Aerospace Center (DLR) to optimize the operational algorithms for validation and eventual data product release. We have also participated in the 2004 Atmospheric Chemistry Validation of Envisat 2 workshop and the 2004 Envisat and ERS Symposium, as well as normal SCIAMACHY meetings.

2.1.1 Algorithm studies

For limb scattering retrievals, an algorithm has been developed to determine cloud top height; it can also provide some information on cloud type. The two brightest wavelengths in channel 6 at the lowest (positive) tangent height (TH) are selected from a given limb scan. These wavelengths are assumed to be non-absorbing and are generally near 1.2 μm. For clear sky conditions, the limb radiance generally increases with decreasing tangent height for these optically thin wavelengths. The cloud top height (if any) is determined by finding the TH corresponding to the maximum in the limb radiance profile at these wavelengths since cloud scattering dominates the signal. The retrieved cloud top height defines the lower altitude of the gas concentration profile retrieval if it is greater than the default lower altitude limit of the retrieval. By default, NO_2 and BrO are retrieved down to ~11 km and OClO is retrieved down to 15 km, so the cloud top height determination is important in tropical profile retrievals where towering clouds can often reach 17 km (see **Figure 1**).

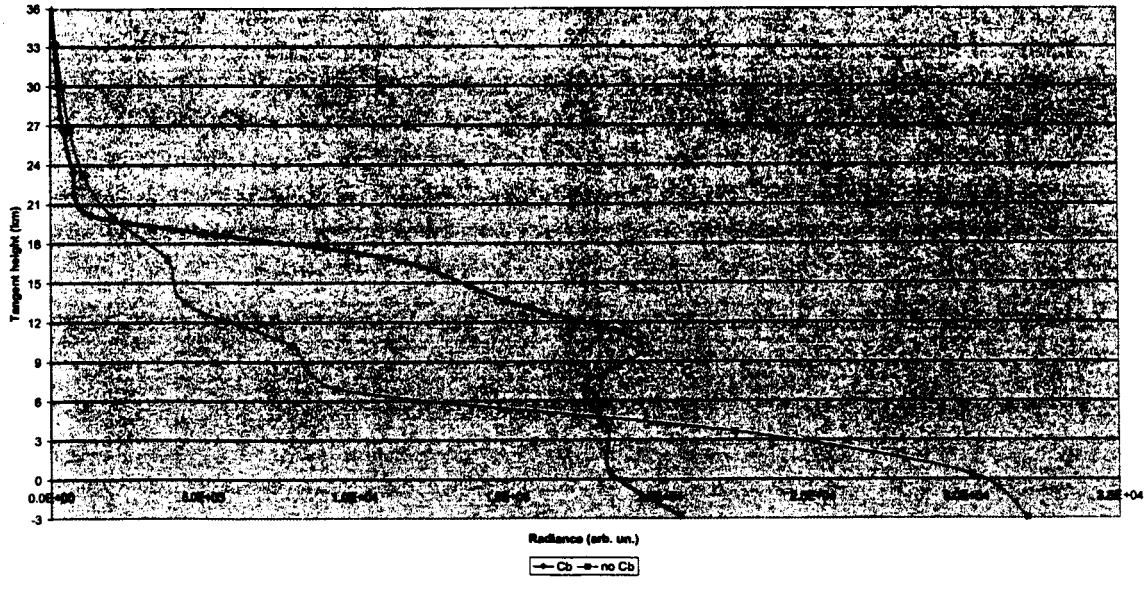

Figure 1. Limb radiance profile at ~1.2 μm observed at 20° S, 38° W in the presence of towering cumulonimbus (Cb) and at 4° N, 44° E (over arid Somalia) in the absence of such clouds on 6 March 2003.

Wavelength calibration

The wavelength calibration method using cross-correlation with a high-resolution Fraunhofer spectrum we introduced for GOME [Caspar and Chance, 1997] is fully implemented for SCIAMACHY at the German Processing and Archiving Centre

(DPAC), for use as a backup for wavelength calibration in case the line calibration lamp fails.

We have taken a standard ATMOS solar reference spectrum, which covers the SCIAMACHY Channel 8 (infrared; CO and N_2O channel), recalibrated it in absolute wavelength to 0.002 cm^{-1} (0.001 nm, or 0.01 SCIAMACHY pixel) using solar CO lines, and supplied it with software to convolve to SCIAMACHY spectral resolution. This solar spectrum is now being used for wavelength calibration as well as for determining undersampling in SCIAMACHY channel 8 (see **Spectral and spatial sampling tests**, below) and to improve the slit function determination as was done previously in the UV-visible (see above reference). The major use at present is in optimizing the fitting algorithm for determination of CO.

Spectral and spatial sampling tests

We initially determined the undersampling correction for the GOME instrument [Chance, 1998] and, with DLR colleagues, improved it for application to SCIAMACHY [Slijkhuis *et al.*, 1999]. We have finished conducting a rigorous analytical study of spectral undersampling which will apply directly to SCIAMACHY, the GOME instruments, OMI, and OMPS (and, presumably, other instruments as well). [Chance *et al.*, 2004a] This improves the correction for undersampling for all of these instruments, and puts it on a firmer theoretical basis. The paper, *"Undersampling Correction for Array Detector-Based Satellite Spectrometers,"* is included as **Appendix A** to this report.

Ring effect studies

We have supplied Ring effect correction spectra to the DLR for use in operational processing of both limb and nadir spectra. In preparation for ozone profile retrievals from high spatial resolution nadir spectra from SCIAMACHY, we have developed a fast real-time Ring effect correction. Further radiometric calibration of the channel 1 and 2 radiance and irradiance is required before realistic ozone profile retrievals will result from the algorithm developed by Liu *et al.* [2004] (**Appendix B** of this report), as applied to GOME data. The Ring effect is not treated in the forward radiative transfer model LIDORT of the retrieval algorithm. A version of LIDORT which accounts for first-order RRS in a multi-layer multiply-scattering atmosphere is available, but it is not preferred because of its high computation cost. Instead, a Ring spectrum is obtained on-line by modeling the first-order RRS of the direct beam [Sioris and Evans, 2000] for the same atmosphere used in the retrieval, accounting for the RRS dependence on viewing geometry and atmospheric ozone and temperature profiles. The Ring spectrum is updated when total O_3 changes by 20 DU from the previous iteration, with the zeroth iteration being the *a priori* O_3 profile. Because multiple scattering is not considered in this model, a scaling parameter is fitted in the retrieval from channel 1 and a 2nd order polynomial scaling is required in channel 2 to account for the large variation in multiple scattering effects especially in the Huggins bands because of the competition between ozone absorption and Rayleigh scattering. We use the actual SCIAMACHY measured solar irradiance instead of a high-resolution reference spectrum because it can reduce the

fitting residual slightly. The Ring spectrum is calculated for a clear-sky atmosphere with an albedo of 0. This Ring model reduces the fitting residual by 15-25% relative to the approach of Chance and Spurr [1997] and increases the DFS by ~0.4 by reducing correlations between the ozone absorption and the filling-in of the ozone lines by rotational Raman scattering. In addition, this on-line Ring calculation is relatively fast, taking negligible computational time compared to forward model calculations with the inelastic version of LIDORT.

Database improvement

We have implemented a full set of UV /visible cross sections to be included HITRAN, as described in Orphal and Chance [2003]; Rothman *et al.* [2003]; Rinsland *et al.* [2003].

2.1.2 Scientific studies

We have provided additional recommendations to the DLR for the SCIAMACHY level 1-2 processing baseline and have performed studies to optimize the operational processing algorithm for several species, including CO (in progress), HCHO (in progress), limb NO_2 (complete last year), limb BrO (complete last year), and limb OClO (in progress).

We have implemented improved methods to determine limb pointing, by using comparisons of measured and modeled "knees" in the limb scattered light, including the use of multiple knees at different wavelengths, and the knee at 305 nm [Sioris *et al.*, 2003]. These approaches have been found to identify and correct for inaccurate pointing information supplied by the satellite to on the order of 300 meters. We have detected the daily drift in pointing which occurs due to an inaccurate on-board orbit model of satellite position and pitch. The drift amounts to 200-300 m per complete orbit. We have also observed the sudden adjustment of SCIAMACHY's pointing which occurs when the orbit model is updated daily near Australia, correcting the >1 km drift which has accumulated over several orbits. We have been able to verify that improvements to the pointing software implemented by ESA have been successful in reducing the pointing drift and also have reduced the scan-to-scan variability of the pointing offset. We find that there is no substantial latitudinal dependence to the pointing on the dayside of the orbit although ESA believes there is a latitudinal dependence of ~800 m amplitude.

We have continued studies (under separate funding) to develop tropospheric data products from SCIAMACHY. We have retrieved tropospheric NO_2 with the limb-nadir matching technique [Sioris *et al.*, 2004]. The stratospheric (and occasionally upper tropospheric) NO_2 profile is retrieved down to:

1. cloud top, or

2. the vertical (2-km) layer below which the uncertainty of the integrated vertical profile above due to including the underlying layer is larger than the resulting increase to the vertical column density.

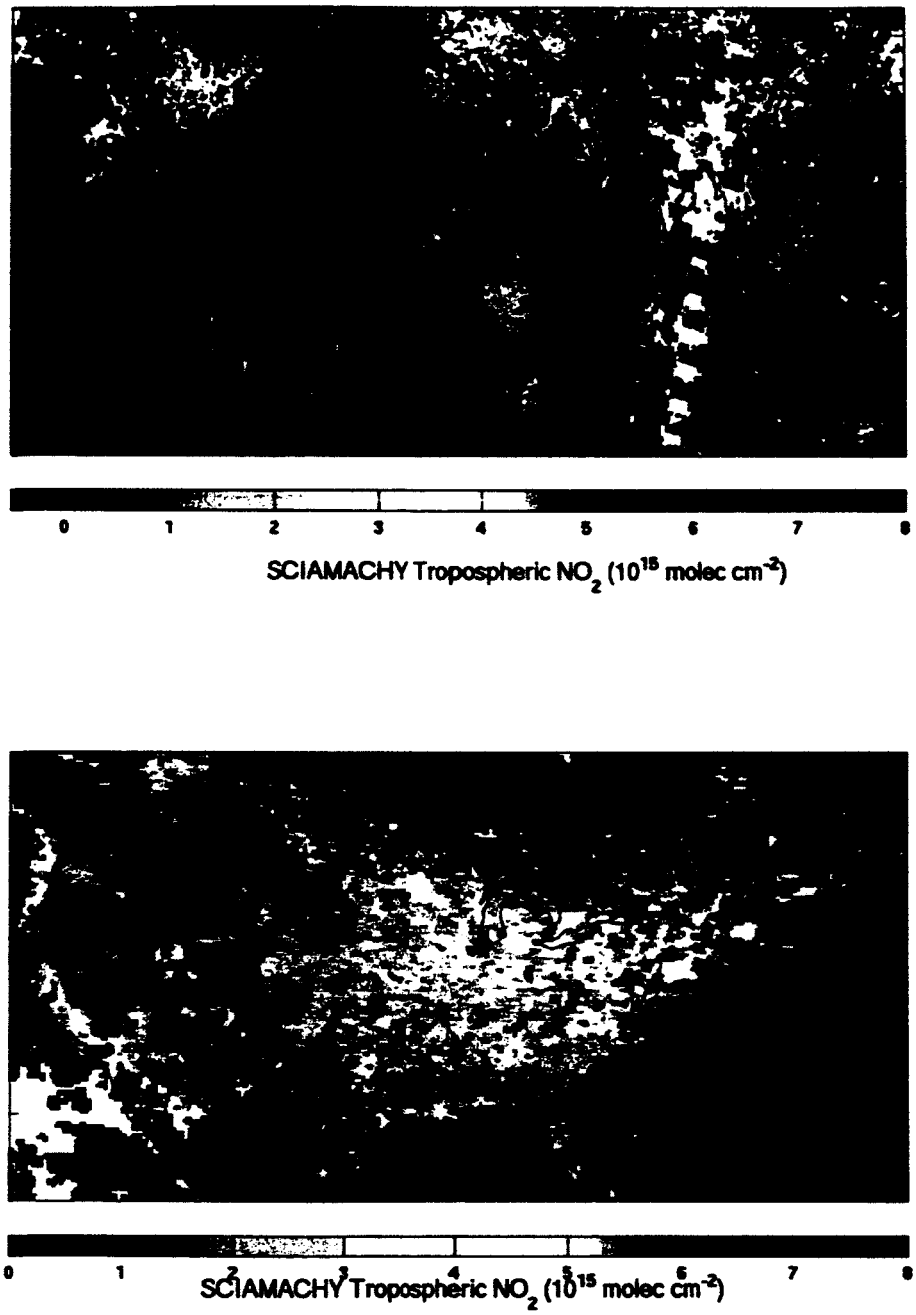

Figure 2. Tropospheric NO_2 derived from SCIAMACHY spectra measured during the 2004 ICART campaign. Top: global tropospheric NO_2. Bottom: Detailed map for North America.

The profile retrieval range is typically 15-41 km. Global retrievals of tropospheric NO_2 continue, with large columns measured over urban centers, and various other sources readily measurable. **Figure 2** is an example of global determination of tropospheric NO_2, and a blow-up of the North American tropospheric NO_2 distribution, during the 2004

International Consortium for Atmospheric Research on Transport and Transformation (ICARTT) campaign.

Tropospheric HCHO determinations are lagging, compared to those from our work on GOME data, because of the need to fully implement improved characterization of the polarization sensitivity into the Level 0-1 algorithm at the operational facility, which has not yet been completed. Preliminary results have been presented at the 2004 COSPAR meeting [Chance *et al.*, 2004b].

CO determination is in progress in collaboration with the Space Research Organization of the Netherlands (SRON). SRON has implemented dark current correction in SCIAMACHY Channel 8 on a per-orbit basis, as well as a dynamic dead- and bad-pixel map. SAO is using their improved calibration to refine the fitting for CO.

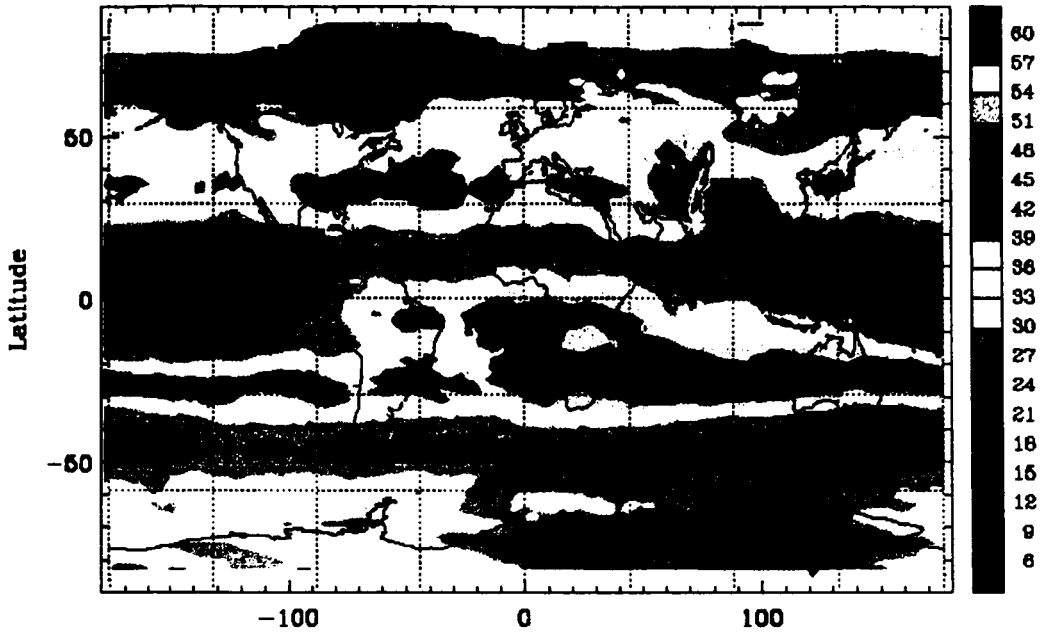

Figure 3. Tropospheric ozone derived from GOME spectra for September 1997. The analysis method, is described in Liu *et al.* 2004.

2.2 GOME Studies

We continue to work with the European Space Agency and Eumetsat, through the GOME Science Advisory Group (GSAG), and the German Aerospace Center (DLR) to optimize the operational algorithms for GOME-2. In particular, we have supplied reference cross section as implemented in HITRAN for use in GOME-2 processing, and have further generalized the method of Fraunhofer cross-correlation for wavelength calibration for use in GOME-2. We continue to participate in GSAG meetings.

Processing and archiving of GOME-1 spectra for BrO, O_3, and HCHO continues. Results are currently available through September 2004. Scientific studies continue under

separate funding [Palmer *et al.*, 2003; Martin *et al.*, 2003; Abbot *et al.*, 2003; Zeng *et al.*, 2003; Jaeglé *et al.*, 2004; Martin *et al.*, 2004].

Substantial progress has been made, under separate funding, on the global determination of tropospheric ozone from GOME-1 measurements [Liu *et al.*, 2004; Chance *et al.*, 2004c]. The Liu *et al.*, 2004 paper is included here as Appendix B. **Figure 3** shows our global retrieval of tropospheric ozone from GOME spectra for the month of September 1997.

2.3 ILAS-II

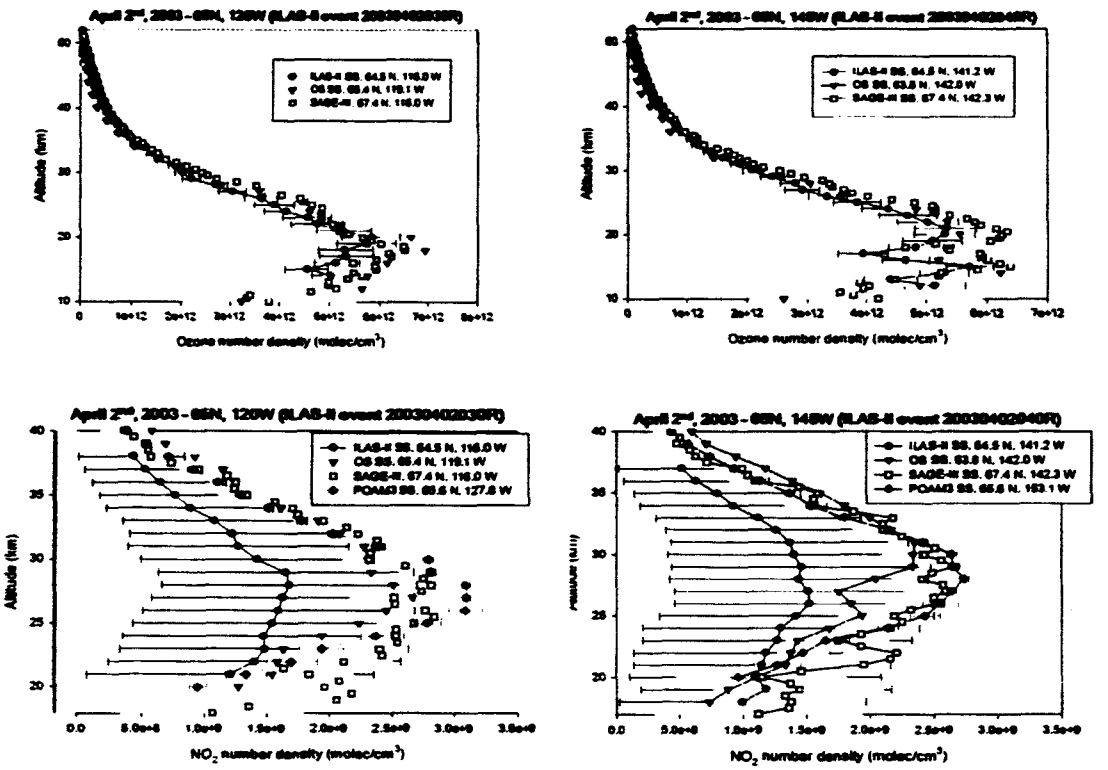

Figure 4. NO_2 and O_3 profiles from ILAS-II, and SAGE-III. Profiles from the POAM-III operational data product, are included for comparison.

ILAS-II work this year focused on first comparisons of NO_2 vertical profiles from ILAS-II with profiles retrieved from SAGE-III, OSIRIS, and SCIAMACHY. The lack of well calibrated SCIAMACHY measurements, and the unfortunate termination of the ILAS-II mission due to the failure of the ADEOS-II satellite on day 300 of 2003 were Limiting factors in these comparisons.

(a) ILAS-II – SCIAMACHY Spatial Coincidences

Comparisons between ILAS-II and SCIAMACHY can be made using both SCIAMACHY solar occultation (northern hemisphere) and limb (northern and southern hemisphere) measurements. SCIAMACHY does not perform any solar occultation

measurements in the southern hemisphere, but rather observes in lunar occultation whenever possible. At the time of the study, comparisons involving SCIAMACHY were limited by the unavailability of well-calibrated data products. Comparisons were also restricted to limb observations (no SCIAMACHY occultation measurements were available), all of which occurred at high solar zenith angles around 97° and so prevented their processing with our limb scatter retrieval program.

A large number of coincidences between ILAS-II and SCIAMACHY (including both limb and solar occultation) can be expected within 4-5° latitude, 12° longitude, and 1 h in time. Restricting observations to a temporal coincidence of 60 min or less, the average difference in observation latitude in April 2003 between ILAS-II and SCIAMACHY was 4.53°.

(b) Comparisons of ILAS-II NO_2 and O_3 Profiles with SAGE-III and OSIRIS

The four plots in **Figure 4** show profiles of NO_2 and O_3 from ILAS-II, and SAGE-III. They also contain profiles from the POAM-III operational data product, which were included for comparison.

This first and preliminary comparison indicates that version 1.00 of the ILAS-II data product is accurately retrieving O_3, while NO_2 seems systematically underestimated compared to the other sensors.

3. Schedule for Third Year

SCIAMACHY Studies

Algorithm studies

- Cloud correction
- Ring effect studies

Scientific studies

- Tropospheric NO_2, HCHO, CO, CH_4, CO_2, and N_2O
- Polar stratospheric cloud measurements

Ongoing GOME-2 studies
Ongoing ILAS-II studies

4. References

Abbot, D.S., P.I. Palmer, R.V. Martin, K. Chance, D.J. Jacob, and A. Guenther, Seasonal and interannual variability of North American isoprene emissions as determined by formaldehyde column emissions from space, *Geophys. Res. Lett.* **30** (17), 1886, doi:10.1029/2003GL017336, 2003.

Caspar C., and K. Chance, GOME wavelength calibration using solar and atmospheric spectra, *Proc. Third ERS Symposium on Space at the Service of our Environment*, Ed. T.-D. Guyenne and D. Danesy, European Space Agency publication SP-414, ISBN 92-9092-656-2, 1997.

Chance, K.V., and R.J.D. Spurr, Ring effect studies: Rayleigh scattering, including molecular parameters for rotational Raman scattering, and the Fraunhofer spectrum, *Appl. Opt.*, **36**, 5224-5230, 1997.

Chance, K., Analysis of BrO measurements from the Global Ozone Monitoring Experiment, *Geophysical Research Letters* **25**, 3335-3338, 1998.

Chance, K. T.P. Kurosu, and C.E. Sioris, Undersampling correction for array detector-based satellite spectrometers, *Applied Optics*, in press, 2004a.

Chance, Kelly, Thomas Kurosu, Robert Spurr, Christopher Sioris, Xiong Liu. Daniel Jacob, Paul Palmer, Dorian Abbot, Randall Martin, Lyatt Jaeglé Yuhang Wang, and Tao Zeng, Satellite-based spectroscopic measurements of tropospheric pollution, Invited presentation to *COSPAR*, 2004b.

Chance, K., X. Liu, C.E. Sioris, R.J.D. Spurr, T.P. Kurosu, R.V. Martin, M.J. Newchurch. and P.K. Bhartia, Ozone profile retrieval from GOME, *XX Quadrennial Ozone Symposium*, 2004c.

Jaeglé, L., R.V. Martin, K. Chance, L. Steinberger, T.P. Kurosu, D.J. Jacob, A.I. Modi, V.Yoboué, L. Sigha-Nkamdjou, and C. Galy-Lacaux, Satellite mapping of rain-induced nitric oxide emissions from soils, *J. Geophys. Res.* **109**, D21310, doi:10.1029/2004JD004787, 2004.

Liu, X., K. Chance, C.E. Sioris, R.J.D. Spurr, T.P. Kurosu, R.V. Martin, M.J. Newchurch, and P.K. Bhartia, Ozone profiles and tropospheric ozone from Global Ozone Monitoring Experiment, *Proc. Envisat & ERS Symposium*, 2004.

Martin, R.M., D.J. Jacob, K. Chance, T. Kurosu, P.I. Palmer, and M.J. Evans, Global inventory of nitrogen oxide emissions constrained by space-based observations of NO_2 columns, *J. Geophys. Res.* **108** (D17), 4537, doi:10.1029/2003JD003453, 2003.

Martin, R.V., D.D. Parrish, T.B. Ryerson, D.K. Nicks Jr., K. Chance, T.P. Kurosu, D.J. Jacob, E.D. Sturges, A. Fried, and B.P. Wert, Evaluation of GOME satellite measurements of tropospheric NO_2 and HCHO using regional data from aircraft campaigns in the southeastern United States, *J. Geophys. Res.*, in press, 2004.

Orphal, J., and K. Chance, Ultraviolet and visible absorption cross sections for HITRAN, *J. Quant. Spectrosc. Radiat. Transfer* **82**, 491-504, 2003.

Palmer, P.I., D.J. Jacob, A.M. Fiore, R.V. Martin, K. Chance, and T. Kuruso, Mapping isoprene emissions over North America using formaldehyde column observations from space, *J. Geophys. Res.* **108**, 4180, doi:10.1029/2002JD002153, 2003.

Rinsland, C.P., J.-M. Flaud, A. Perrin, M. Birk, G. Wagner, A. Goldman, A. Barbe, M.-R. De Backer-Barilly, S.N Mikhailenko, Vl.G. Tyuterev, M.A.H. Smith, V.M. Devi, D.C. Benner, F. Schreier, K.V. Chance, J. Orphal, and T. M. Stephen, Spectroscopic parameters for ozone and its isotopes: recent measurements, outstanding issues, and prospects for improvements to HITRAN, *J. Quant. Spectrosc. Radiat. Transfer* **82**, 207-218, 2003.

Rothman, L.S., A. Barbe, D.C. Benner, L.R. Brown, C. Camy-Peyret, M.R. Carleer, K. Chance, C. Clerbaux, V. Dana, V.M. Devi, A. Fayt, J.-M. Flaud, R.R. Gamache, A. Goldman, D. Jacquemart, K.W. Jucks, W.J. Lafferty, J.-Y. Mandin, S.T. Massie, V. Nemtchinov, D.A. Newnham, A. Perrin, C.P. Rinsland, J. Schroeder, K.M. Smith, M.A.H. Smith, K. Tang, R.A. Toth, J. Vander Auwera, P. Varanasi, and K. Yoshino, The HITRAN molecular spectroscopic database: Edition of 2000 including updates through 2001, *J. Quant. Spectrosc. Radiat. Transfer* **82**, 5-44, 2003.

Sioris, C.E. and W.F.J. Evans, Impact of rotational Raman scattering on the O_2 *A* band, *Geophys. Res. Lett.*, **27**, 4085-4088, 2000.

Sioris, C.E., C.S. Haley, C.A. McLinden, C. von Savigny, I.C. McDade, W.F.J. Evans, J.C. McConnell, N.D. Lloyd, E.J. Llewellyn, D. Murtagh, U. Frisk, T.P. Kurosu, K.V. Chance, K. Pfeilsticker, H. Bösch, and F. Weidner, Stratospheric profiles of nitrogen dioxide observed by Optical Spectrograph and InfraRed Imager System on the Odin satellite, *Journal of Geophysical Research*, **108**, 4215, doi:10.1029/2002JD002672, 2003.

Sioris, C.E., T.P. Kurosu, R.V. Martin and K. Chance, Stratospheric and tropospheric NO_2 observed by SCIAMACHY: First results, *Adv. Space Res. Special issue: Trace Constituents in the Troposphere and Lower Stratosphere*, **34/4**, 780-785, 2004.

Slijkhuis, S., A. von Bargen, W. Thomas, and K. Chance, Calculation of undersampling correction spectra for DOAS spectral fitting, *Proc. ESAMS'99 - European Symposium on Atmospheric Measurements from Space*, 563-569, 1999.

Zeng, T., Y. Wang, K. Chance, E.V. Browell, B.A. Ridley, and E.L. Atlas, Widespread persistent near-surface O3 depletion at northern high latitudes in spring, *Geophys. Res. Lett.* **30** (24), 2298, doi:10.1029/2003GL018587, 2003

Appendix A

Undersampling Correction for Array Detector-Based Satellite Spectrometers

Undersampling Correction for Array Detector-Based Satellite Spectrometers

Kelly Chance, Thomas P. Kurosu, and Christopher E. Sioris

Harvard-Smithsonian Center for Astrophysics, 60 Garden Street, Cambridge, MA 02138, USA

Array detector-based instruments are now fundamental to measurements of ozone and other atmospheric trace gases from space in the ultraviolet, visible, and infrared. The present generation of such instruments suffers, to a greater or lesser degree, from undersampling of the spectra, leading to difficulties in the analysis of atmospheric radiances. We provide extended analysis of the undersampling suffered by modern satellite spectrometers, which include GOME, SCIAMACHY, OMI, and OMPS. The analysis includes basic undersampling, the effects of binning into separate detector pixels, and the application of high-resolution Fraunhofer spectral data to correct for undersampling in many useful cases.

OCIS codes: 010.1280, 120.4570, 280.1120

1. Introduction

Array-based spectrometers used in atmospheric remote sensing can suffer substantially from spectral undersampling, with negative consequences to the quality of data retrieved from the

measurements. This was first obvious in measurements from the Global Ozone Monitoring Experiment (GOME),[1] where scientists fitting trace gases from GOME spectra found quite large systematic fitting residuals, and large fitting errors, even after correcting for Doppler shifts between radiances and irradiances. Ref. 2 recognized that this was mainly due to spectral undersampling and presented a technique for correcting most (>90%) of the *undersampling error* in spectral regions where atmospheric absorption effects are small. For GOME, this includes fitting regions used for nitrogen dioxide (NO_2), bromine monoxide (BrO), chlorine dioxide (OClO), and formaldehyde (HCHO). If used with caution, the technique can also be applied successfully to O_3 and SO_2. (Caution is required because the absorption optical depths for O_3 are higher than for the other trace species listed; correction assumes that, to first order, the radiance spectrum consists mostly of back scattered Fraunhofer structure. The SO_2 absorption occurs in the region where O_3 also absorbs strongly.) The technique consists of comparing fully-sampled and undersampled versions of a high resolution Fraunhofer reference spectrum,[3] with the difference being the effect of undersampling. Ref. 4 suggested that the observed residuals are induced by the resampling required to compare Earth radiance and solar irradiance spectra in the fitting, because they are measured with different Doppler shifts of the ERS-2 satellite with respect to the sun. It is demonstrated here that this is not entirely the case: Wavelength shifts between GOME radiances and irradiances are larger than can be accounted for by Doppler shifts. Ref 4 also presented a version of the technique of Ref. 2 implemented in the Scanning Imaging Absorption Spectrometer for Atmospheric Chartography (SCIAMACHY) operational processor. The technique is now also used for measurement of HCHO[5] and NO_2,[6] and has been implemented in the operational processor for measurements of BrO, OClO, and HCHO by the Ozone Monitoring Instrument (OMI).[7]

The present analysis improves on the previous understanding of correction for undersampling by fully considering the sampling theorem in conjunction with the instrument slit function. The analysis is applied to measurements by GOME and OMI, since they represent the two major instrument types: diode array detectors (GOME) and CCD detectors (OMI). The development applies as well to other instruments, including SCIAMACHY (diode array detectors) and the Ozone Mapping and Profiler Suite (OMPS), part of the National Polar Orbiting Environmental Satellite System (NPOESS), which uses CCD detectors.

2. Definitions and Assumptions

The spectrometers considered here use array detectors, which respond to the incoming light over finite regions, with defined response profiles. We will use the term instrument line shape (ILS) for the response of a spectrometer to a monochromatic source up to where it enters the array detector, and the term instrument transfer function (ITF) for the ILS convolved with the detector pixel response. The following properties are assumed to be valid over the region of the array detector that is necessary to consider for ITFs and undersampling corrections at a given pixel, as developed here.

1. **Linear response**. Each pixel responds linearly to input light intensity.
2. **Equal pixel response**. Pixels respond equally to photons of different wavelength. Pixels respond (or can be calibrated to respond) equally in output signal for equal input light intensity.
3. **Linear dispersion**. Pixel wavelengths are at equal increments.
4. **No endpoint issues**. The region under consideration is sufficiently far from the array end for wavelengths beyond the array wavelength range to contribute to the signal.

(Proximity to the array end would require re-calculation of the ILS from deconvolution of the ITF, as discussed below.)

5. **Calibration light source issues**. Instrument transfer functions (ITFs) are determined using either:
    - Lines with negligible spectral width or;
    - A tunable source with negligible spectral width and equal intensity as it is tuned over the ITF.
6. **Slit width variation** is negligible over the ITF centered at each particular wavelength.

Higher-order corrections will likely be needed in the future to account for the breakdown of some of these assumptions.

3. Spectral Undersampling

Consider a wavelength range extending from λ_{min} to λ_{max} that is fully or partly sampled by an array of detectors, spaced at wavelength increment $\delta\lambda$. Any continuous incoming signal spectrum extending over the wavelength range can be represented fully by expansion in spatial (*i.e.*, wavelength) frequency in a Fourier series:

$$S(\lambda) = a_0 + \sum_{k=1}^{\infty}[a_k \cos kt + b_k \sin kt] = a_0 + \sum_{k=1}^{\infty}[a_k \cos(\omega_k(\lambda - \lambda_{min})) + b_k \sin(\omega_k(\lambda - \lambda_{min}))], \quad (1)$$

(1)

where

$$t = 2\pi \frac{\lambda - \lambda_{min}}{\lambda_{max} - \lambda_{min}} \equiv 2\pi \frac{\lambda - \lambda_{min}}{\Delta\lambda}, \quad (2)$$

and the spatial frequencies are:

$$\omega_k = \frac{2\pi k}{\Delta\lambda}. \quad (3)$$

Suppose that the signal is *band-limited*, that is, limited in content of spatial frequency components to a maximum spatial frequency ω_{max}. Then, by the *sampling theorem*,[8,9] the information content of the spectrum is fully known if the spectrum is sampled over the full range λ_{min} to λ_{max} to twice this maximum spatial frequency, $2\omega_{max}$ (the *Nyquist sampling frequency*):

$$\frac{\delta\lambda}{2\pi} = \frac{1}{2\omega_{max}}. \tag{4}$$

In this case, the signal expansion includes only the terms necessary to measure spatial frequencies $\leq \omega_{max}$:

$$S(\lambda) = a_0 + \sum_{k=1}^{N} [a_k \cos kt + b_k \sin kt], \quad N = \frac{\Delta\lambda}{2\delta\lambda}. \tag{5}$$

The spectrum is *completely* determined by this expansion. Its values at points other than the sampled points can be determined using the fact that the value at each sampled point λ_n represents the intensity c_n of a sampling function, sinc $[2\pi\ (\lambda_n - \lambda) / \delta\lambda]$, centered at that point,[8]

$$\text{sinc}[2\pi(\lambda_n - \lambda)/\delta\lambda] = \frac{\sin[2\pi(\lambda_n - \lambda)/\delta\lambda]}{[2\pi(\lambda_n - \lambda)/\delta\lambda]}, \tag{6}$$

plus the constant offset a_0:

$$c_n = S(\lambda_n) - a_0 = \sum_{k=1}^{N} [a_k \cos kt_n + b_k \sin kt_n], \quad t_n = \frac{2\pi(\lambda_n - \lambda_{\min})}{\Delta\lambda} \tag{7}$$

The sampling function is written here in this way to emphasize the pixel dependence and orientation of the following discussion. The sampling function presented here is actually an approximation to a fuller and more complex form,[9,10] but the difference amounts to a completely negligible correction except within several sample points of the λ_{min} and λ_{max} endpoints.

If the signal is not band-limited to ω_{max} but is still sampled to only $2\omega_{max}$, spatial frequencies greater than ω_{max} are *aliased* into the band $0 < \omega \leq \omega_{max}$, with signal information for

$\omega_{max} < \omega \leq 2\omega_{max}$ appearing at $\omega_{max} - \omega$, information for $2\omega_{max} < \omega \leq 3\omega_{max}$ appearing at $\omega - 2\omega_{max}$, *etc.* (Ref. 9, pp. 16-18). It will be demonstrated later that information aliased from the spatial frequency band $\omega_{max} < \omega \leq 2\omega_{max}$ represents the most important sources of problems for GOME, and the main target of corrections. Problems from aliasing in the spectra become most evident when it becomes necessary to resample a spectrum in wavelength, for example when comparing an atmospheric radiance spectrum with a solar irradiance spectrum to determine atmospheric composition from molecular absorption lines, but the interference from aliasing is present in any case when the spectrum is undersampled (*i.e.*, the spectrum is not fully Nyquist sampled). For example, synthetic spectra calculated during the fitting process to determine abundances of atmospheric gases would not normally include aliasing, while the measured spectra would.

A Nyquist-sampled spectrum $S(\lambda)$ is fully described by summing over the contributions from the m individual sample points:

$$S(\lambda) = c_0 + \sum_{i=1}^{m} c_i \,\mathrm{sinc}[2\pi(\lambda_i - \lambda)/\delta\lambda]. \tag{8}$$

It is now possible to investigate the case where the spectrum is not fully Nyquist sampled. Consider a spectrum input to the instrument $S_{inp}(\lambda)$. If the spectrum is completely known *a priori*, it can be expanded as before in a Fourier series

$$S_{inp}(\lambda) = a_0 + \sum_{k=1}^{\infty} [a_k \cos kt + b_k \sin kt]. \tag{9}$$

S_{inp} can be separated into a Nyquist-sampled part, S_{nyq}, containing only spatial frequencies $\leq \omega_{max}$, and an undersampled part, S_{und}:

$$S_{nyq}(\lambda) = a_0 + \sum_{k=1}^{N} [a_k \cos kt + b_k \sin kt], \tag{10a}$$

$$S_{und}(\lambda) = \sum_{k=N+1}^{\infty} [a_k \cos kt + b_k \sin kt]. \qquad (10b)$$

The undersampled part of the spectrum is thus

$$S_{und}(\lambda) = S_{inp}(\lambda) - \sum_{i=1}^{m} c_i \,\mathrm{sinc}[2\pi(\lambda_i - \lambda)/\delta\lambda] - c_0,$$

(11)

where m runs over the sampled points.

4. Slit Functions (Instrument Transfer Functions)

An ITF serves as a low-pass filter to limit the spatial frequency content of the spectrum. Ideally, an ITF would limit the spectral information to frequencies $\leq \omega_{max}$. The ITFs for satellite-based spectrometers are measured in one of three manners:

1. By using a reference line lamp (often a PtNeCr lamp[11]). This method has the advantage that lamp lines are much narrower than the ITF. The disadvantages are that lines are not always completely separated, that spectral coverage may be inadequate in some regions, and that a set of points (one per detector pixel) is mapped out, rather than a continuous ITF. This method was used for GOME and SCIAMACHY.
2. By using a tunable source consisting of a broadband light source and a monochromator. This method has the advantage of mapping out a continuous ITF, but the disadvantage of being a spectrally broader source than the PtNeCr line source. This method was used for OMI, where the full-width at half-maximum (FWHM) of the source was $\leq$ 0.1 OMI detector pixel (M. Dobber and R. Dirksen, *private communication*, 2003). The residual effects from finite source width could, in principle, be reduced using the deconvolution techniques introduced below.

3. By fitting flight spectral irradiance data to a high-resolution solar reference spectrum,[3] where the fitting includes wavelength adjustment and simultaneous fitting to a parameterized ITF.[2,12]

An ITF, $\Gamma(\lambda)$, can be expanded to include Nyquist-sampled and undersampled portions, ignoring (for now) detector pixel binning:

$$\Gamma(\lambda) = \gamma_0 + \sum_{i=a}^{b} \gamma_i \,\mathrm{sinc}[2\pi(\lambda_i - \lambda)/\delta\lambda] + \Gamma_{und}(\lambda). \tag{12}$$

The limits *a* and *b* are selected to include portions of the detector array where the slit function contributes significantly. As examples, we show the Gaussian GOME ITF we normally use for wavelength calibration purposes. A more complex, compound hypergeometric, ITF was determined during the instrument characterization.[13] We find that the Gaussian spectrum provides better wavelength calibration for GOME spectra, and is used routinely in our data analyses. It also provides much better undersampling correction for GOME spectral fitting. We show an OMI ITF (M. Dobber and R. Dirksen, *private communication*, 2003) for this same wavelength region, and for the NO_2 fitting region (405-465 nm; the ITF determined at 432 nm is used here). The OMI ITFs are selected for CCD row 150, corresponding to a viewing azimuth angle of 29.5°, about half way from the nadir view to the extremity of the OMI swath. Additional types of ITFs for OMI may be considered once there is flight data for comparison. For all ITFs shown in this section, the complication of binning over the detector pixel response function is not yet included. This will be discussed in a later section.

Figure 1 shows the GOME Gaussian ITF, determined from ERS-2 orbit 81003031 (October 3, 1998), used here as a test orbit for determination of undersampling correction, appropriate to the fitting window used for BrO retrieval in GOME.[2] The FWHM of the ITF is 0.160 nm, and there are 1.4 samples per FWHM in this region of GOME spectra. The ITF is

additionally decomposed into fully-sampled and undersampled components. Figure 2 shows this ITF with the hypothetical sampling to twice the GOME sampling frequency. Figure 3 shows the OMI ITF for this same wavelength region (FWHM = 0.421 nm, 2.8 samples per FWHM), and its decomposition into fully-sampled and undersampled components. Figure 4 shows this ITF with the hypothetical sampling to twice the OMI sampling frequency. Figures 5 and 6 show the OMI ITFs and decompositions for the NO_2 fitting wavelength range (FWHM = 0.639 nm, 3.0 samples per FWHM). Note the asymmetry in the measured OMI ITFs and their decompositions.

It is clear from all three examples that higher sampling by a factor of 2 greatly decreases the undersampled portion of the ITF, almost eliminating undersampling. Since for GOME this corresponds to 2.8 samples per FWHM, this demonstrates that information aliased from the spatial frequency band $\omega_{max} < \omega \leq 2\omega_{max}$ represents the most important source of undersampling in this spectral region.

5. Binning into Detector Pixels

GOME and SCIAMACHY use Reticon-S RL-1024 SRU-type linear diode array detectors, which are designed to have the sensitivity profiles shown in Figure 7 for the spectral resolution and sampling of GOME. These detectors have 1024 photodiode elements spaced at 25 μm. The center 13 μm of each element is n-doped, with the bulk of the material p-doped, to generate the response profile shown (the newer Reticon-L detectors are also spaced at 25 μm, but with 19 μm n-doped regions and 6 μm interdiode gaps).

Characterization of the actual pixel responses must take into account the fact that the input light source (mostly Fraunhofer spectrum, convolved with the ILS) varies significantly across the detector pixel profile. The final response is the integral across the pixel profile of the convolution of the input spectrum with the ILS:

$$R_{pix}(\lambda) = \int_{profile} S(\lambda') \otimes \Gamma(\lambda - \lambda') d\lambda', \tag{13}$$

where R_{pix} is the pixel response, S is the input spectrum, Γ is the ILS, and $\otimes$ denotes convolution. In order to calculate the response, it is first necessary to obtain the ILS by *deconvolution*, since the measured ITF is the convolution of the ILS with the pixel response profile. This is accomplished using the *Jansson method*, as described in Ref. 14, for GOME, and a nonlinear least squares fitting to a parameterized profile shape for OMI. The result for the GOME slit function is shown in Figure 8. The deconvolved slit is the best match to the ILS that could be obtained in the iterative deconvolution process. The difference between the initial and reconvolved slit is an indicator of the goodness-of-fit for this procedure. The response functions for the OMI CCD detectors are Gaussian with a full-width at half maximum of 25 μm and separated by 22.5 μm (M. Dobber and R. Dirksen, *private communication*, 2003). Figures 9 and 10 show these along with the decomposition to determine the ILS for the BrO and NO_2 fitting regions of OMI.

6. Undersampling Correction

6.1 Wavelength calibration issues

Satellite radiances and irradiances can be calibrated in wavelength with high absolute accuracy (typically ≤0.0004 nm for the GOME BrO fitting region) using cross-correlation to the solar spectrum of Ref. 3, with simultaneous fitting of the ITF.[2,12] Ref. 2 suggested that the apparent wavelength shift between GOME radiances and irradiances was due to instrumental effects, influencing the way the detectors are illuminated in the different measuring geometries. Ref. 4 stated that it is due to the Doppler effect, since irradiances are obtained during the portion of the

orbit when the satellite is moving toward the sun. For ERS-2 orbit 81003031, the maximum velocity toward the sun is 7.46 km s^{-1}, while the average wavelength shift (irradiance – radiance) for the BrO fitting window is equivalent to 7.865±0.025 km s^{-1} (0.00923±0.00003 nm). The satellite Doppler shift contributes 6.89 km s^{-1} (0.0081 nm), rather than the full 7.46 km s^{-1}, given the GOME solar measurement procedure.[4] There is an additional component of 0.50 km s^{-1} at this season from the ellipticity of the Earth's orbit, for a total Doppler shift of 7.39 km s^{-1}, leaving a significant instrument and/or spectral component (see the discussion in Ref. 15 for possible spectral "tilt" contributions). For the other spectrometers considered here, the relative contributions are not yet determined. For OMI in particular, since its undersampling is calculated here, a relative shift equal to the full Doppler shift is assumed; this will be modified when flight data become available.

6.2 Undersampling calculations

Calculation of the undersampling correction for each case is accomplished by convolving the high spectral resolution (0.01 nm) solar reference spectrum of Ref. 3 with the ITF determined for the instrument and wavelength region, and differencing fully-sampled and undersampled representations of this convolved solar spectrum at the sampling grid of the satellite radiances:

1. Convolve the high resolution solar reference spectrum E_{ref} with the satellite instrument ITF to create a lower spectral resolution, but highly oversampled, solar reference spectrum, E_{over}:

$$E_{over}(\lambda) = \int_{profile} E_{ref}(\lambda') \otimes ITF(\lambda - \lambda') d\lambda' . \qquad (14)$$

The portion of E_{ref} used in fitting BrO for GOME is shown in Figure 11, top panel; E_{over} for this spectral region is shown in Figure 11, middle panel.

2. Determine from direct cross-correlation (for GOME) or estimate (for OMI) the wavelength grids for irradiance and radiance spectra g_{irr} and g_{rad}.
3. Sample E_{over} at the wavelength grid g_{irr}, to give E_{irr}, and at the grid g_{rad}, to give E_{rad}, using cubic spline interpolation[16] to determine values at each exact grid point. These are now undersampled representations of the solar reference spectrum, although each is correct *at the points on its sampling grid.* E_{irr} is shown in Figure 11, bottom panel; E_{rad} is virtually indistinguishable when over-plotted.
4. Resample E_{irr} to the wavelength grid g_{rad}, using cubic spline interpolation, giving E'_{rad}.
5. The undersampling correction C_u, in optical thickness units, is the difference between E_{rad} and E'_{rad}, normalized to the average of E_{rad} over the fitting window:

$$C_u(\lambda) = \frac{E_{rad}(\lambda) - E'_{rad}(\lambda)}{\bar{E}_{rad}}. \qquad (15)$$

C_u corresponds to differencing fully-sampled and undersampled representations of the convolved solar spectrum since only E_{irr} is resampled, thus inducing undersampling error on the radiance wavelength grid g_{rad}. This undersampling correction assumes that, to first order, the radiance spectrum consists mostly of back scattered Fraunhofer structure. Higher-order corrections could be made to account for atmospheric absorption and the Ring effect. Figure 12 shows the residuals from fitting for BrO (without the use of an undersampling spectrum as a basis function) in ERS-2 orbit 81003031 for a measurement pixel midway through the orbit (pixel 800) and as an orbit average (top panel); the bottom panel shows the undersampling C_u calculated here for the average relative wavelength shift between irradiance and radiance fitted for this orbit (0.0092 nm). The calculated undersampling correction accounts for more than 90% of the fitting residuals. Figure 13, top panel, shows the undersampling calculated for the OMI baseline BrO fitting window, assuming a relative radiance-irradiance shift corresponding to the full Doppler

shift for the Aura orbit (7.5 km s^{-1}). The bottom panel shows the absorption for a typical BrO slant column density of 1×10^{14} cm^{-2}. The units (optical thickness and transmission) are equivalent in scale for these small interferences and absorptions. The undersampling correction is roughly an order of magnitude smaller than for GOME, but is still larger than the BrO absorption and needs to be carefully included in the fitting of the satellite data. Figure 14, top panel, shows the undersampling calculated for the OMI baseline NO_2 fitting window, assuming a relative radiance-irradiance shift corresponding to the full Doppler shift for the Aura orbit. The bottom panel shows the absorption for a typical NO_2 North American summer slant column density of 1.25×10^{16} cm^{-2}. The contribution is less severe but, at ca. 20% of the nominal NO_2 signal, it is still by no means negligible. Undersampling correction will very likely need to be included in order to derive meaningful tropospheric NO_2 abundances from OMI measurements. Under heavily polluted conditions over North America in summertime, for example, the tropospheric contribution to the NO_2 slant column usually does not exceed 40%.[6] Effective monitoring of moderate pollution requires correction to substantially better than that level.

An attempt was made to improve the undersampling correction for GOME by calculation of the undersampling spectrum for the deconvolved ILS, followed by convolution of the resulting spectrum with the Reticon response function. The result of this procedure was expected to be an improved undersampling correction which would correspond even more closely to the GOME fitting residual, as shown in Figure 12, top panel. The actual result was substantially worse. The magnitude was approximately correct, but the spectral details were not. We think that the reason is that the actual detector response function deviates considerably from the trapezoidal shape shown in Figure 7. For the present, at least, the best undersampling corrections continue to be those determined using the entire ITF. These are shown in Figures 12, 13, and 14. When OMI

flight data become available, this procedure will be attempted to see whether it provides improved undersampling correction for this case.

7. Discussion and Conclusions

We provide a method that may be used to simply and reliably estimate the degree of undersampling an instrument configuration will have. For instruments where the ITF may be approximated as Gaussian (GOME), we show that sampling at 2.8 pixels/FWHM will almost completely eliminate undersampling. For more complex ITFs (OMI), significant undersampling can exist at 3.0 pixels/FWHM.

Undersampling for ground-based, zenith-sky spectrometers has been discussed in Ref. 17 in the context of measuring O_3, NO_2, and NO_3. On the basis of numerical experiments, it is recommend to use sampling ratios between 4.5 and 6.5 pixels/FWHM, for Gaussian ITFs, to avoid undersampling. This is consistent with our finding that for OMI NO_2 measurements undersampling will be significant, and will highly impact tropospheric NO_2 measurements, at 3.0 pixels/FWHM, but that at 6.0 pixels/FWHM it becomes negligible. The improvement in undersampling of OMI over that of GOME is due to the higher sampling rates (2.8 and 3.0 samples per FWHM for the OMI UV and visible examples versus 1.4 for the GOME UV example). Asymmetric ITFs such as those of OMI and perhaps other imaging spectrometers may require higher sampling ratios than symmetric ITFs.

The previously developed undersampling correction[2,4] is now commonly used in GOME scientific analyses and has been implemented operationally for SCIAMACHY. It has been demonstrated here that correction will be required for OMI BrO and tropospheric NO_2 measurements, at least. Complete implementation will not be possible until the ITFs and

irradiance-radiance wavelength shifts are characterized in flight versus CCD row. A similar conclusion almost certainly applies to the OMPS instruments.

Further refinement of the undersampling correction for OMI, to include full averaging of the solar spectrum over the ILS and convolution with the pixel response is currently in progress, to be ready for application to flight spectra. For GOME, this further refinement has been shown not to be an improvement, likely due to incorrect characterization of the Reticon response function. Convolution with the ITF followed by the sampling procedure described above in **Undersampling calculations** provides very accurate correction.

Higher order corrections for instrumental effects, such as uneven sampling in wavelength space, and spectroscopic effects, such as atmospheric absorption and the Ring effect, may eventually be developed if analysis of flight data indicates that they are warranted.

Acknowledgements

This research was funded by the National Aeronautical and Space Administration and the Smithsonian Institution. We thank Marcel Dobber and Ruud Dirksen of the KNMI and Ruud Hoogeveen of the SRON for help with information on GOME and OMI detector responses and ITF determinations. It is always a pleasure to acknowledge the European Space Agency and the German Aerospace Center for their ongoing cooperation in GOME and SCIAMACHY.

References

1. European Space Agency, "The GOME Users Manual," ed. F. Bednarz, European Space Agency Publication SP-1182, ESA Publications Division, ESTEC, Noordwijk, The Netherlands, ISBN-92-9092-327-x (1995).

2. K. Chance, Analysis of BrO measurements from the Global Ozone Monitoring Experiment. *Geophys. Res. Lett.* **25**, 3335-3338 (1998).

3. K.V. Chance and R.J.D. Spurr, Ring effect studies: Rayleigh scattering, including molecular parameters for rotational Raman scattering, and the Fraunhofer spectrum, *Appl. Opt.* **36**, 5224-5230 (1997).

4. S. Slijkhuis, A. von Bargen, W. Thomas, and K. Chance, Calculation of undersampling correction spectra for DOAS spectral fitting, Proc. ESAMS'99 - European Symposium on Atmospheric Measurements from Space, 563-569 (1999).

5. K. Chance, P.I. Palmer, R.J.D. Spurr, R.V. Martin, T.P. Kurosu, and D.J. Jacob, Satellite observations of formaldehyde over North America from GOME, *Geophys. Res. Lett.* **27**, 3461-3464 (2000).

6. R.V. Martin, K. Chance, D.J. Jacob, T.P. Kurosu, R.J.D. Spurr, E. Bucsela, J.F. Gleason, P.I. Palmer, I. Bey, A.M. Fiore, Q. Li, and R.M. Yantosca, An improved retrieval of tropospheric nitrogen dioxide from GOME, *J. Geophys. Res.* **107**, 4437, doi:10.1029/2001JD0010127 (2002).

7. NASA, "OMI Algorithm Theoretical Basis Document Volume 4: Trace Gas Algorithms," ed. K. Chance (2002). Available at `http://eospso.gsfc.nasa.gov/eos_homepage/for_scientists/atbd/`

8. S. Goldman, "Information Theory," Prentice-Hall, NY (1953).

9. R.W. Hamming, "Digital Filters," Prentice-Hall, Englewood Cliffs, NJ, ISBN 0-13-212571-4 (1977).

10. J.C. Brasunas, Jr., "Far-Infrared Spectroscopy of Gaseous Nebulae," Ph.D. Thesis, Department of Physics, Harvard University (1981).

11. J.E. Murray, "Atlas of the Spectrum of a Platinum/Chromium/Neon Hollow-Cathode Reference Lamp in the Region 240-790 nm," ESA Report (1994).

12. C. Caspar and K. Chance, GOME wavelength calibration using solar and atmospheric spectra, *Proc. 3rd ERS Symposium on Space at the Service of our Environment*, ed. T.-D. Guyenne and D. Danesy, European Space Agency publication SP-414, ISBN 92-9092-656-2 (1997).

13. R. Spurr and W. Thomas, GOME software databases for level 1 to 2 processing, ER-TN-IFE-GO-0018, Iss./Rev.3/A (2002). Available at http://earth.esa.int/services/esa_doc/doc_gom.html

14. W.E. Blass and G.W. Halsey, "Deconvolution of Absorption Spectra," Academic Press, NY, ISBN 0-12-104650-8 (1981).

15. C.E. Sioris, C.S. Haley, C.A. McLinden, C. von Savigny, I.C. McDade, W.F.J. Evans, J.C. McConnell, N.D. Lloyd, E.J. Llewellyn, D. Murtagh, U. Frisk, T.P. Kurosu, K.V. Chance, K. Pfeilsticker, H. Bösch, and F. Weidner, Stratospheric profiles of nitrogen dioxide observed by Optical Spectrograph and Infrared Imager System on the Odin satellite, *J. Geophys. Res.* **108**, No. D7, 4215, doi:10.1029/2002JD002672 (2003).

16. W.H. Press, P.B. Flannery, S.A. Teukolsky, and W.A. Vetterling, "Numerical Recipes," Cambridge University Press, ISBN 0-521-30811-9 (1986).

17. H.K. Roscoe, D.J. Fish, and R.L. Jones, Interpolation errors in UV-visible spectroscopy for stratospheric sensing: Implications for sensitivity, spectral resolution, and spectral range, *Appl. Opt.* **35**, 427-432 (1996).

Figure Captions

Fig. 1 GOME Gaussian instrument transfer function in the spectral region used for bromine monoxide determinations, and its decomposition into Nyquist-sampled and undersampled components.

Fig. 2 GOME Gaussian instrument transfer function and the Nyquist-sampled and undersampled portions for the hypothetical case where the slit function is sampled to twice the GOME spatial frequency.

Fig. 3 OMI instrument transfer function for the BrO fitting region and the Nyquist-sampled and undersampled portions.

Fig. 4 OMI instrument transfer function for the BrO fitting region and the Nyquist-sampled and undersampled portions for the hypothetical case where the slit function is sampled to twice the OMI spatial frequency.

Fig. 5 OMI instrument transfer function for the NO_2 fitting region and the Nyquist-sampled and undersampled portions.

Fig. 6 OMI instrument transfer function for the NO_2 fitting region and the Nyquist-sampled and undersampled portions for the hypothetical case where the slit function is sampled to twice the OMI spatial frequency.

Fig. 7 Response of three Reticon-S detector pixels as a function of location in GOME detector channel 2.

Fig. 8 Deconvolution of the GOME ITF from the pixel response function to determine the ILS in the BrO fitting region.

Fig. 9 Deconvolution of the OMI ITF from the pixel response function to determine the ILS in the BrO fitting region.

Fig. 10 Deconvolution of the OMI ITF from the pixel response function to determine the ILS in the NO_2 fitting region.

Fig. 11 The portion of the high resolution solar reference spectrum E_{ref} used in fitting BrO for GOME (top); E_{ref} convolved with the GOME ITF to create the lower spectral resolution, but highly oversampled, solar reference spectrum, E_{over} (middle); E_{over} sampled at the wavelength grid of the GOME irradiance (E_{irr}) (bottom). E_{irr} and E_{rad} (not plotted here; see text) are undersampled representations of the solar reference spectrum.

Fig. 12 Residuals from fitting GOME spectra for BrO in ERS-2 orbit 81003031, for a single spectrum and as an average for all spectra in the orbit (top); Synthetic undersampling, C_u, calculated here for the relative wavelength shift between the GOME irradiance and the GOME radiance (bottom).

Fig. 13 Synthetic OMI undersampling, C_u, in the BrO fitting region, calculated here for a relative wavelength shift of the irradiance and radiance corresponding to 7.5 km s^{-1} (top); absorption for a typical BrO slant column density of 1×10^{14} cm^{-2} (bottom).

Fig. 14 Synthetic OMI undersampling, C_u, in the NO_2 fitting region, calculated here for a relative wavelength shift of the irradiance and radiance corresponding to 7.5 km s^{-1} (top); absorption for a typical NO_2 slant column density of 1.25×10^{16} cm^{-2} (bottom).

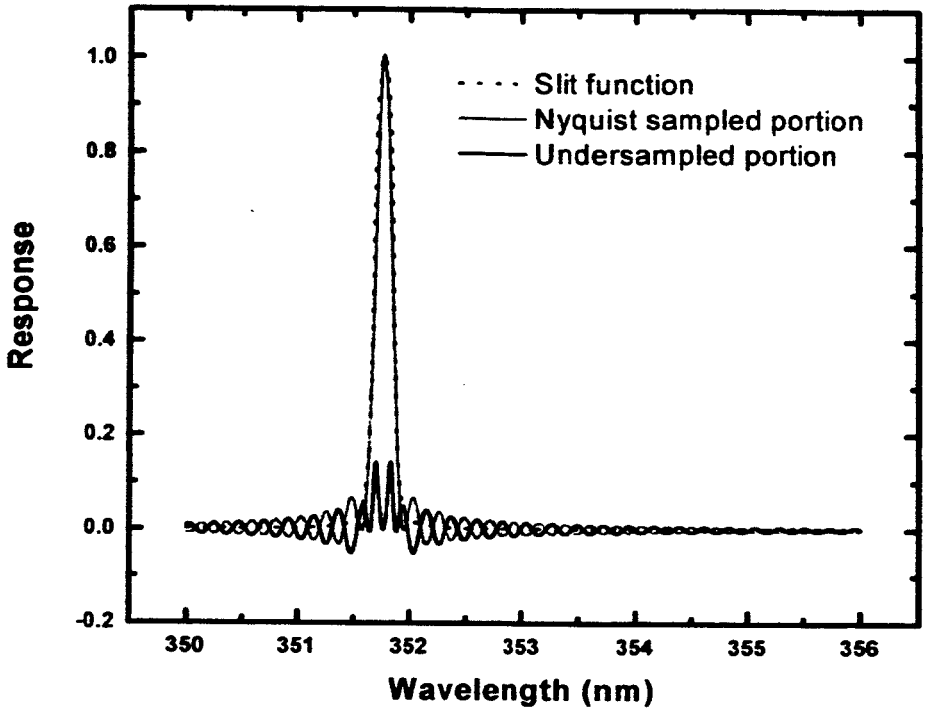
Slit function
Nyquist sampled portion
Undersampled portion
Response
1.0
0.8
0.6
0.4
0.2
0.0
-0.2
350
351
352
353
354
355
356
Wavelength (nm)

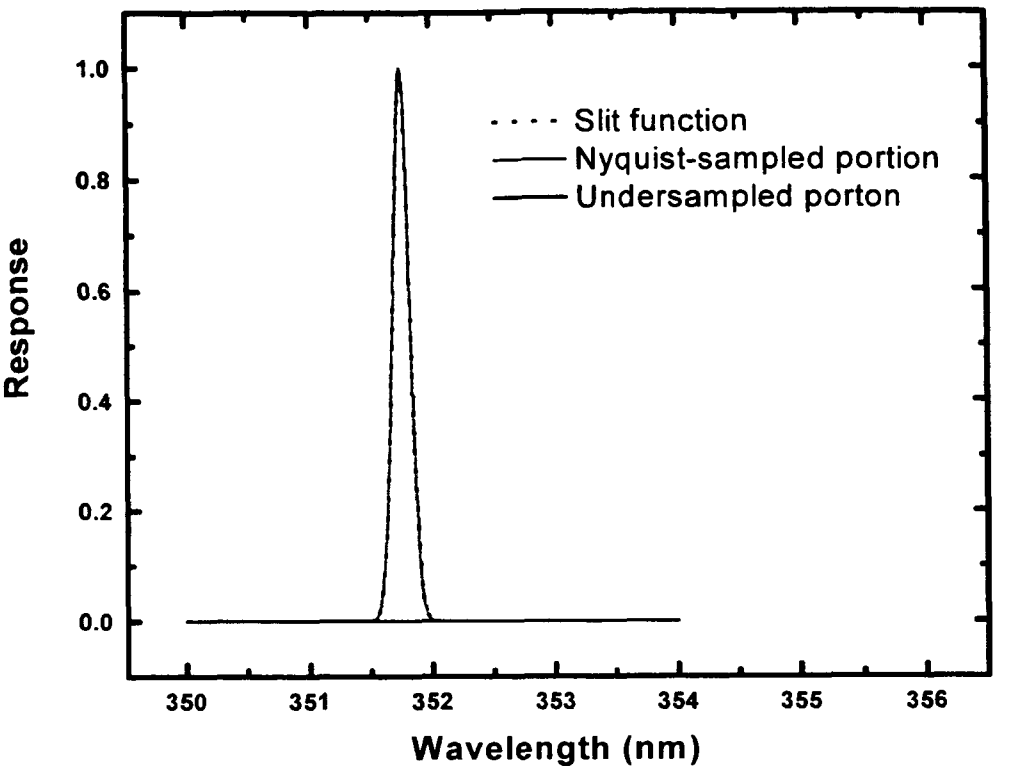
Response
1.0
0.8
0.6
0.4
0.2
0.0
350
351
352
353
354
355
356
Wavelength (nm)
Slit function
Nyquist-sampled portion
Undersampled porton

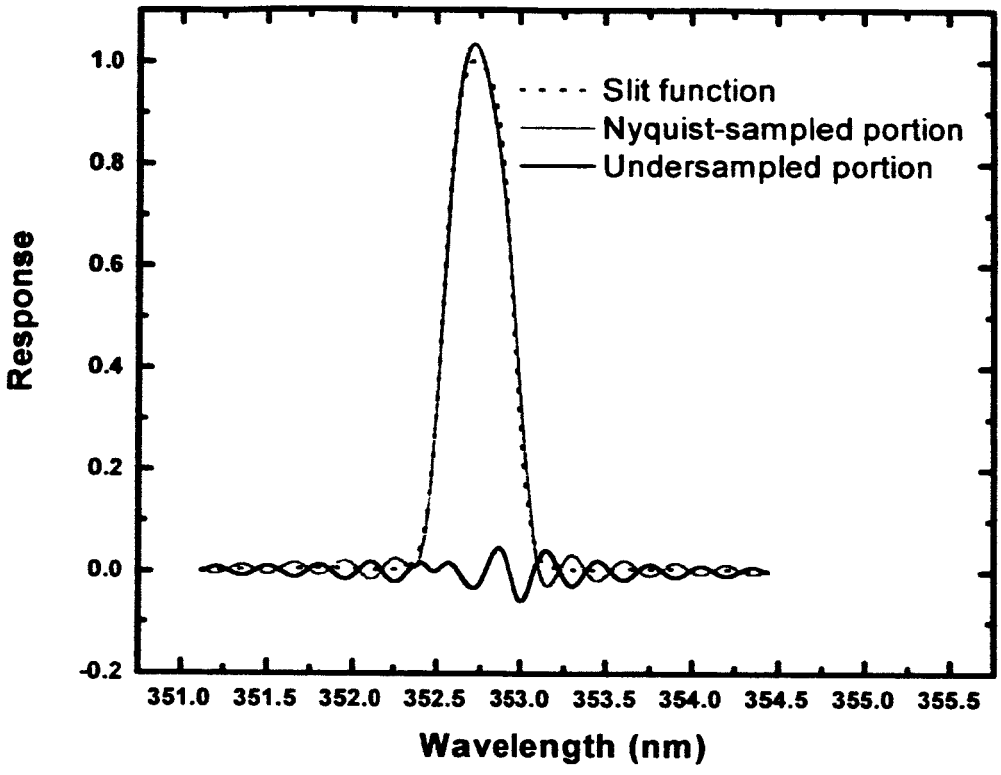
Slit function
Nyquist-sampled portion
Undersampled portion
Response
1.0
0.8
0.6
0.4
0.2
0.0
-0.2
351.0
351.5
352.0
352.5
353.0
353.5
354.0
354.5
355.0
355.5
Wavelength (nm)

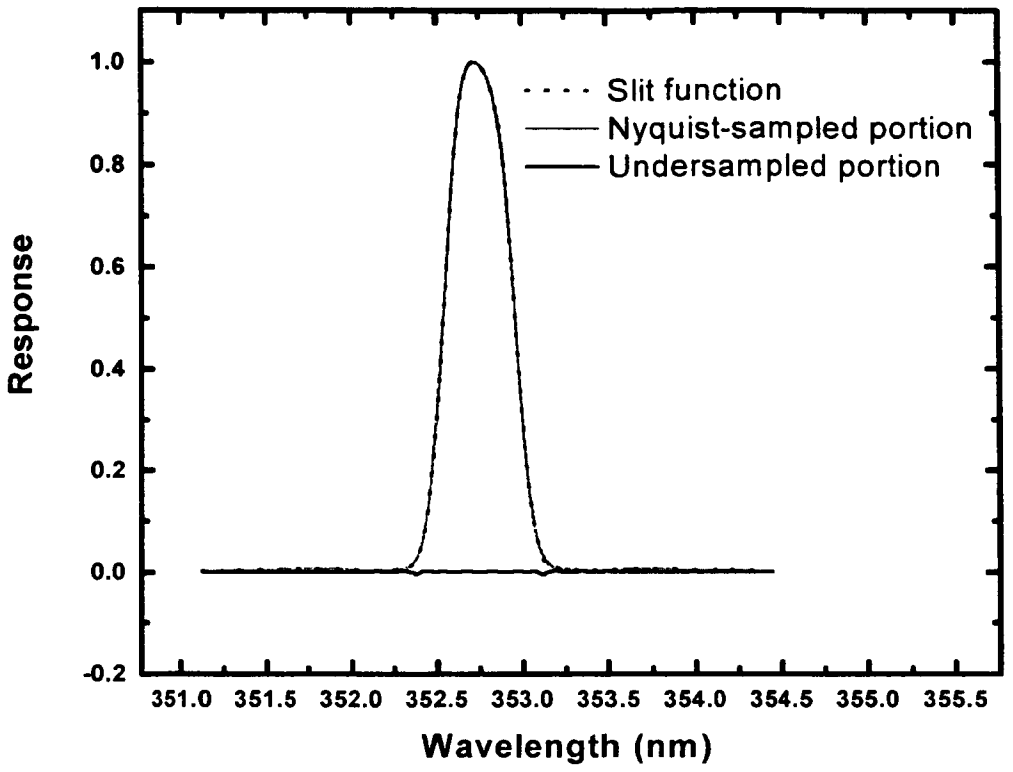
Slit function
Nyquist-sampled portion
Undersampled portion
Response
1.0
0.8
0.6
0.4
0.2
0.0
-0.2
351.0
351.5
352.0
352.5
353.0
353.5
354.0
354.5
355.0
355.5
Wavelength (nm)

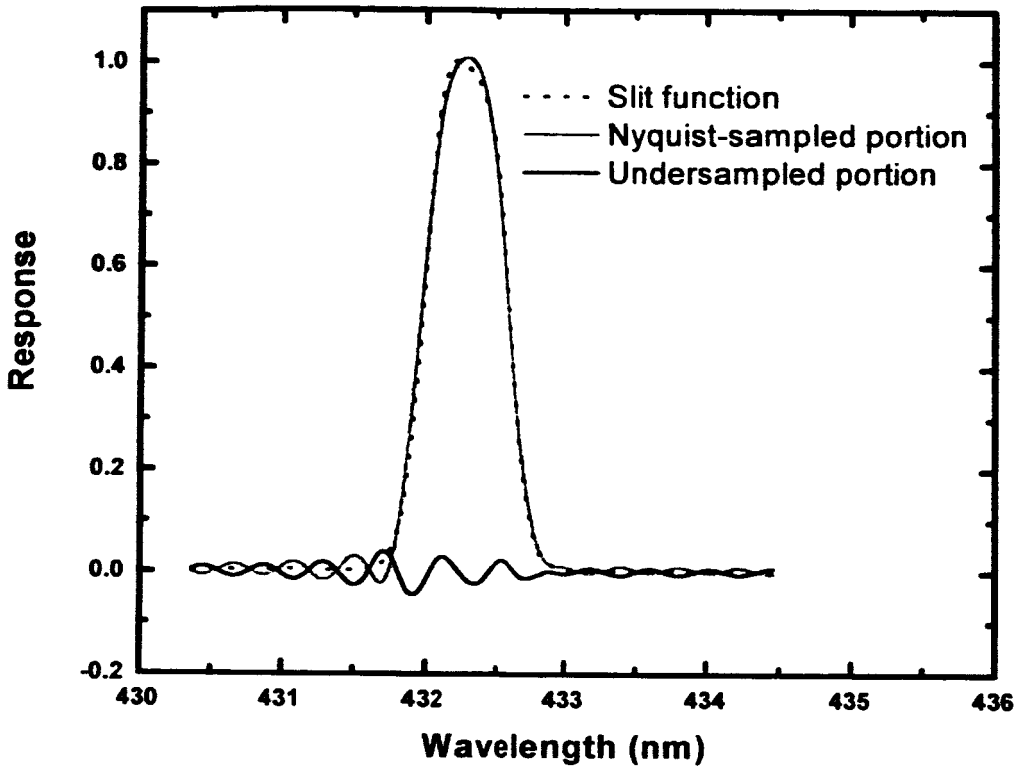
Slit function
Nyquist-sampled portion
Undersampled portion
Response
1.0
0.8
0.6
0.4
0.2
0.0
-0.2
430
431
432
433
434
435
436
Wavelength (nm)

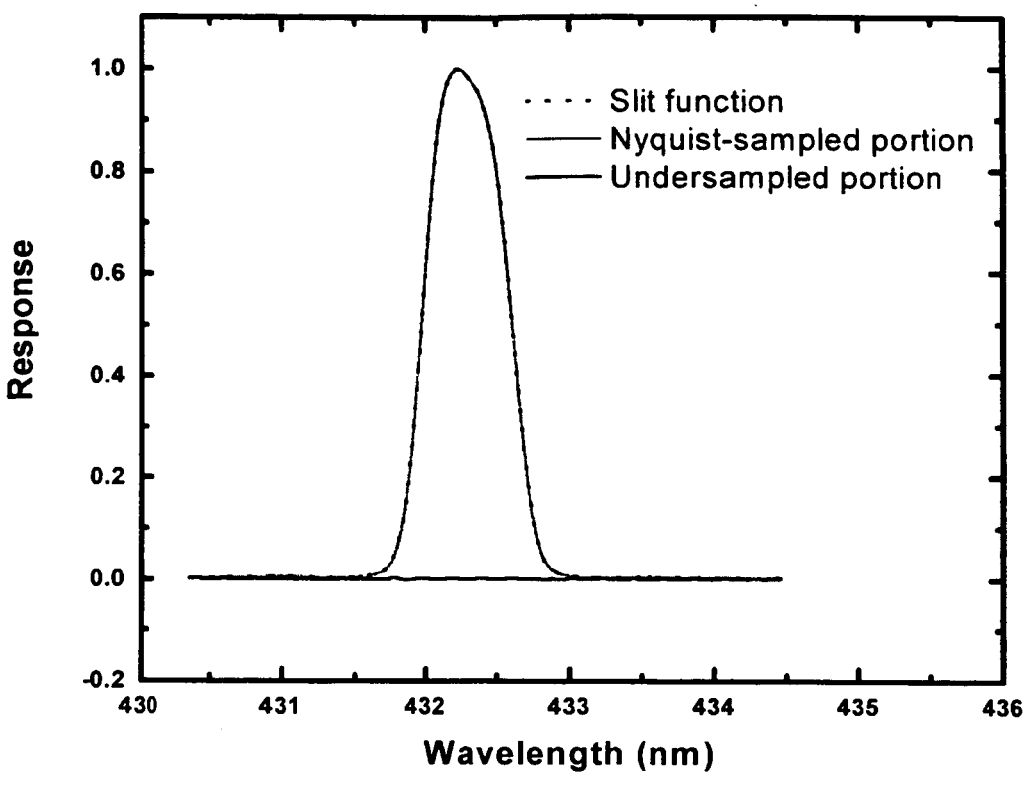
Response
1.0
0.8
0.6
0.4
0.2
0.0
-0.2
430
431
432
433
434
435
436
Wavelength (nm)
Slit function
Nyquist-sampled portion
Undersampled portion

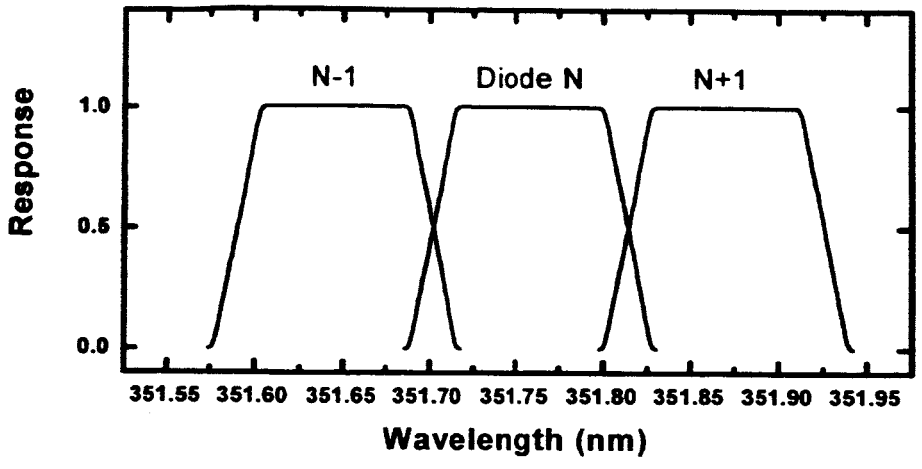
N-1
Diode N
N+1
Response
1.0
0.5
0.0
351.55 351.60 351.65 351.70 351.75 351.80 351.85 351.90 351.95
Wavelength (nm)

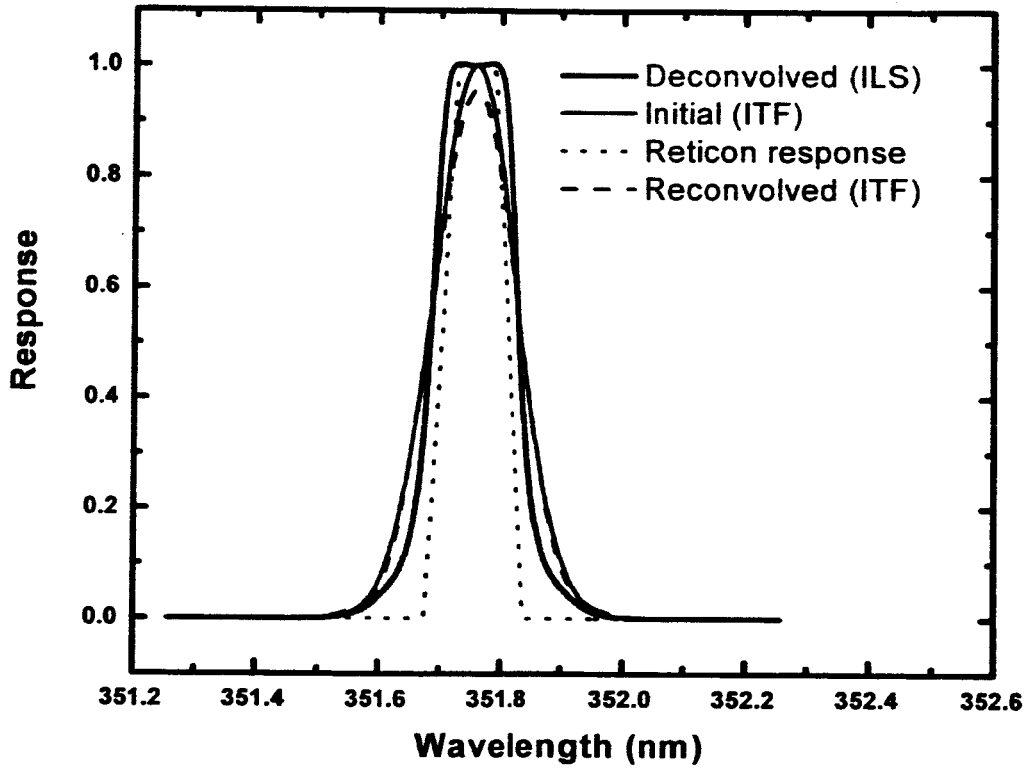
Deconvolved (ILS)
Initial (ITF)
Reticon response
Reconvolved (ITF)
Response
1.0
0.8
0.6
0.4
0.2
0.0
351.2 351.4 351.6 351.8 352.0 352.2 352.4 352.6
Wavelength (nm)

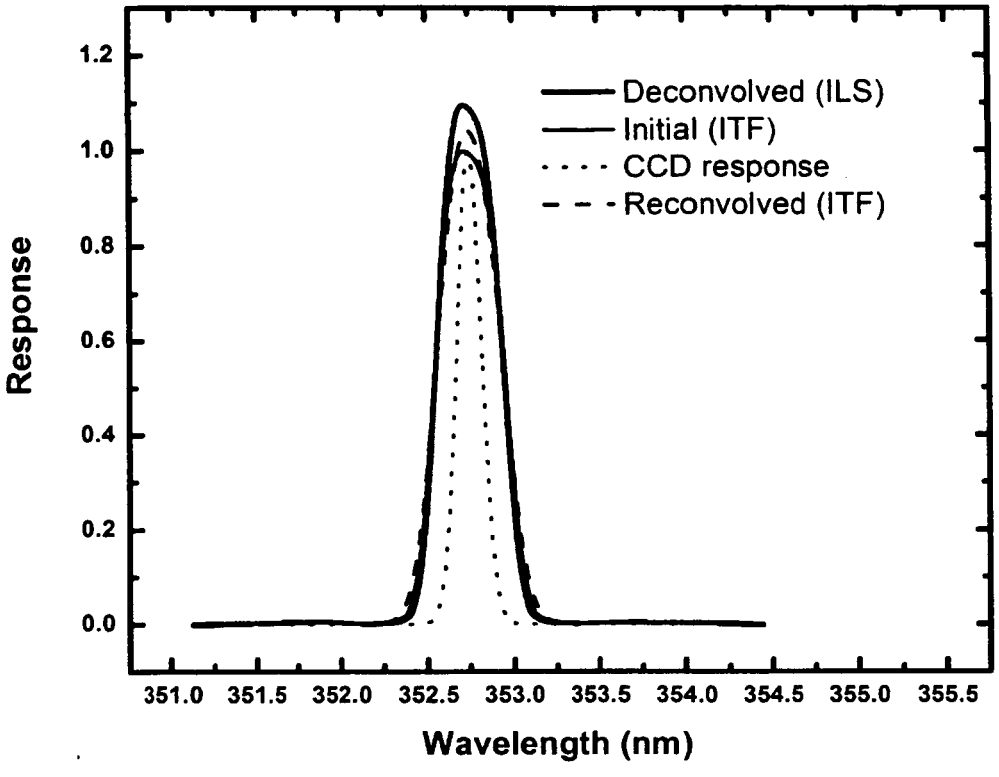
Deconvolved (ILS)
Initial (ITF)
CCD response
Reconvolved (ITF)
Response
1.2
1.0
0.8
0.6
0.4
0.2
0.0
351.0
351.5
352.0
352.5
353.0
353.5
354.0
354.5
355.0
355.5
Wavelength (nm)

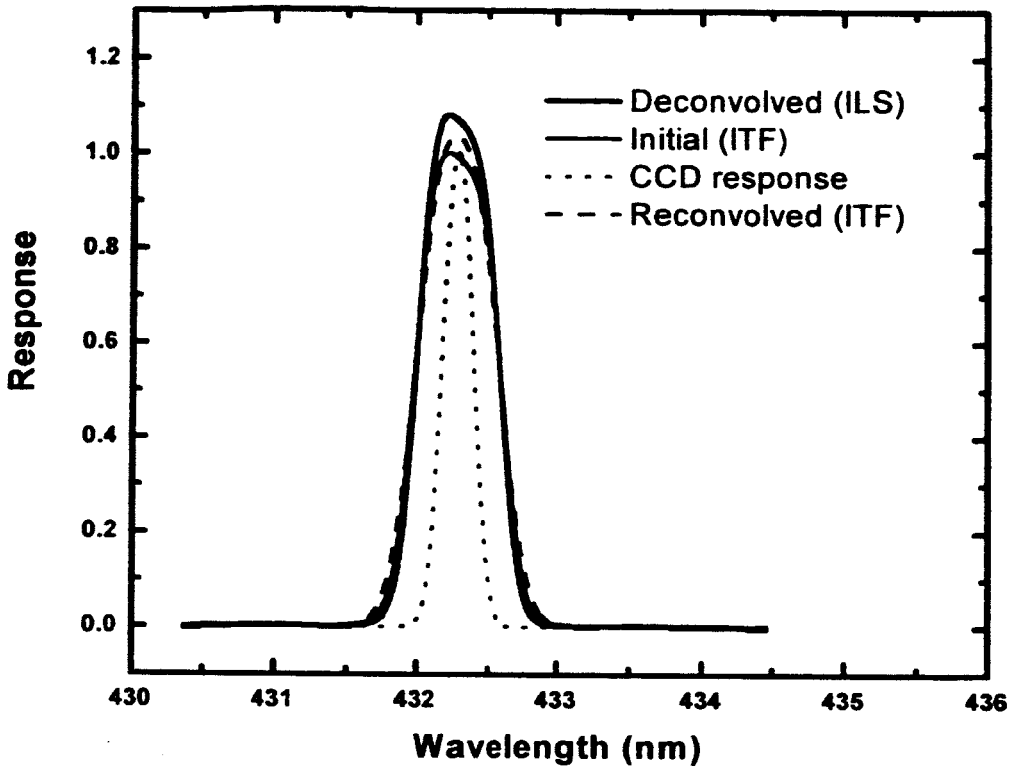
Deconvolved (ILS)
Initial (ITF)
CCD response
Reconvolved (ITF)
Response
Wavelength (nm)
0.0
0.2
0.4
0.6
0.8
1.0
1.2
430
431
432
433
434
435
436

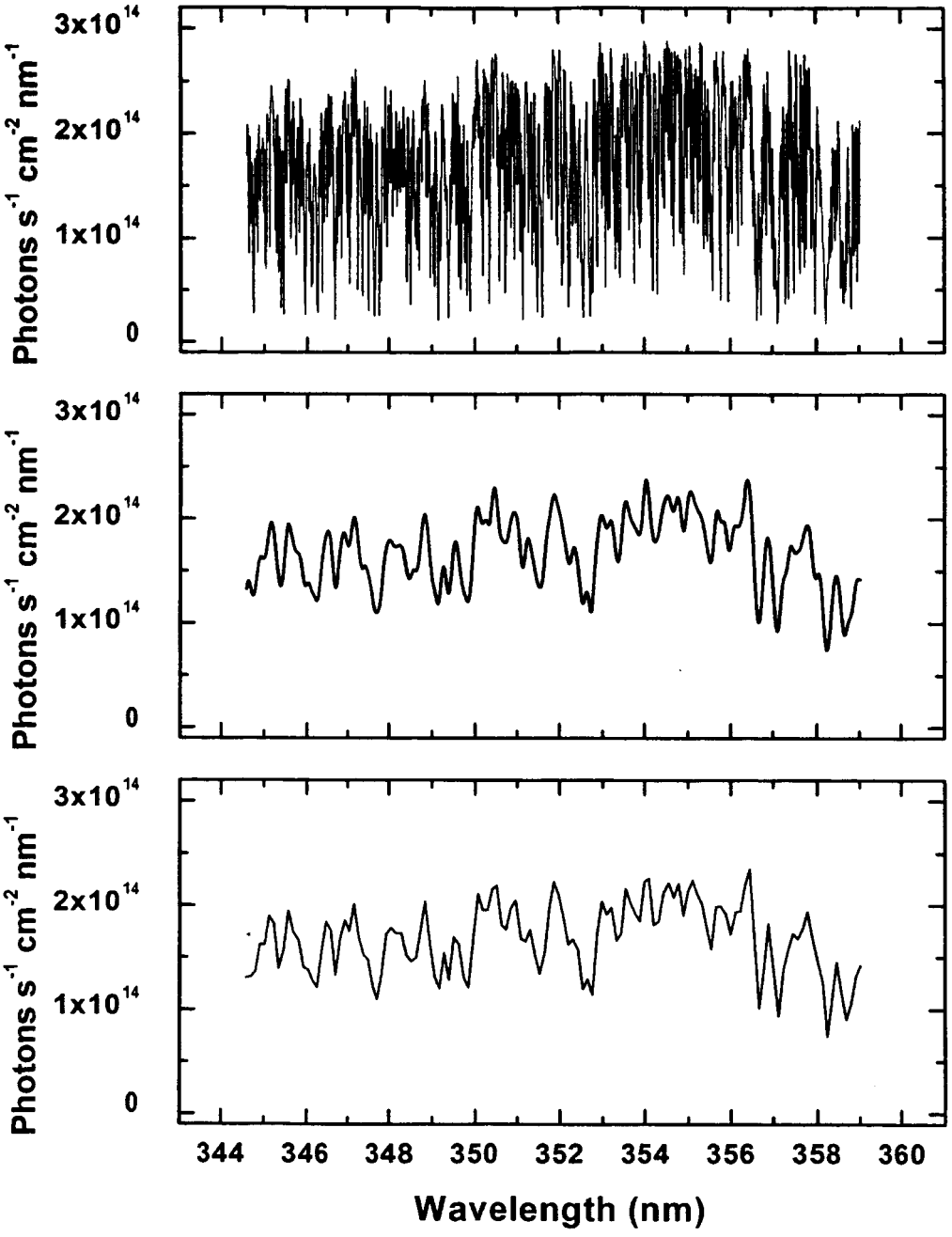
3x10^14
2x10^14
1x10^14
0
Photons s^-1 cm^-2 nm^-1
344
346
348
350
352
354
356
358
360
Wavelength (nm)

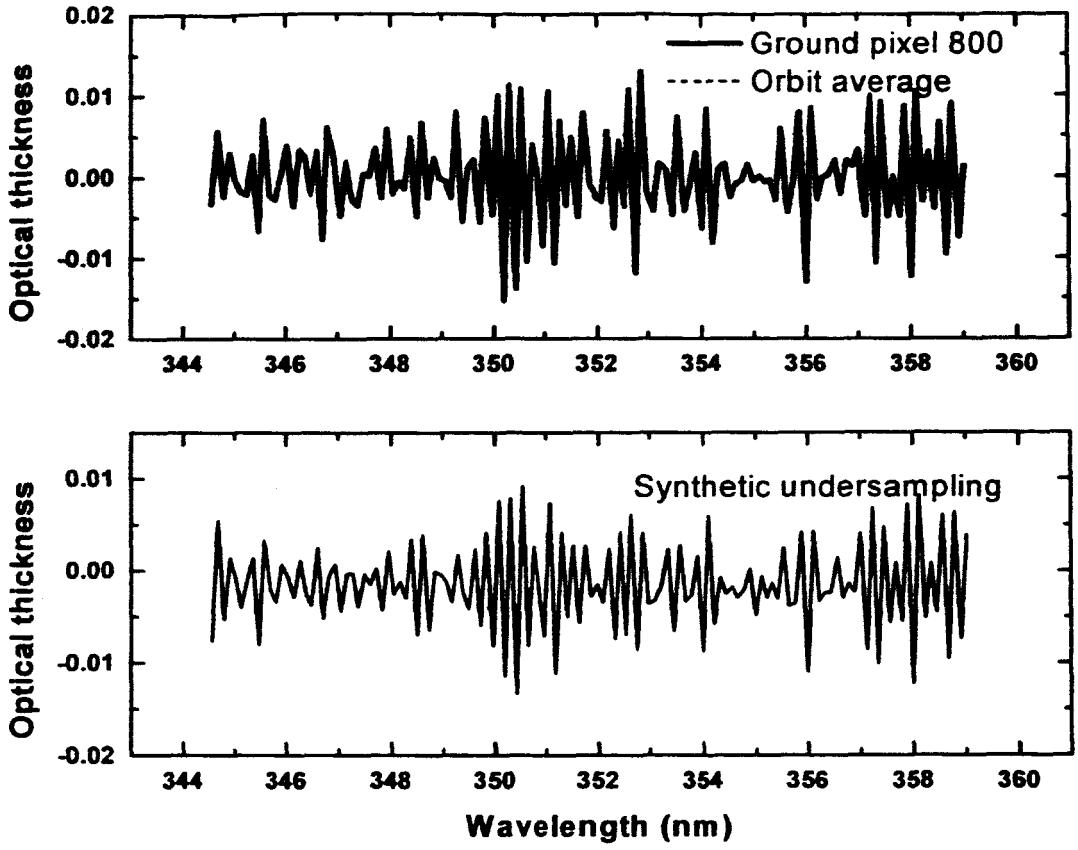
Ground pixel 800
Orbit average
Optical thickness
0.02
0.01
0.00
-0.01
-0.02
344
346
348
350
352
354
356
358
360
Synthetic undersampling
Optical thickness
0.01
0.00
-0.01
-0.02
344
346
348
350
352
354
356
358
360
Wavelength (nm)

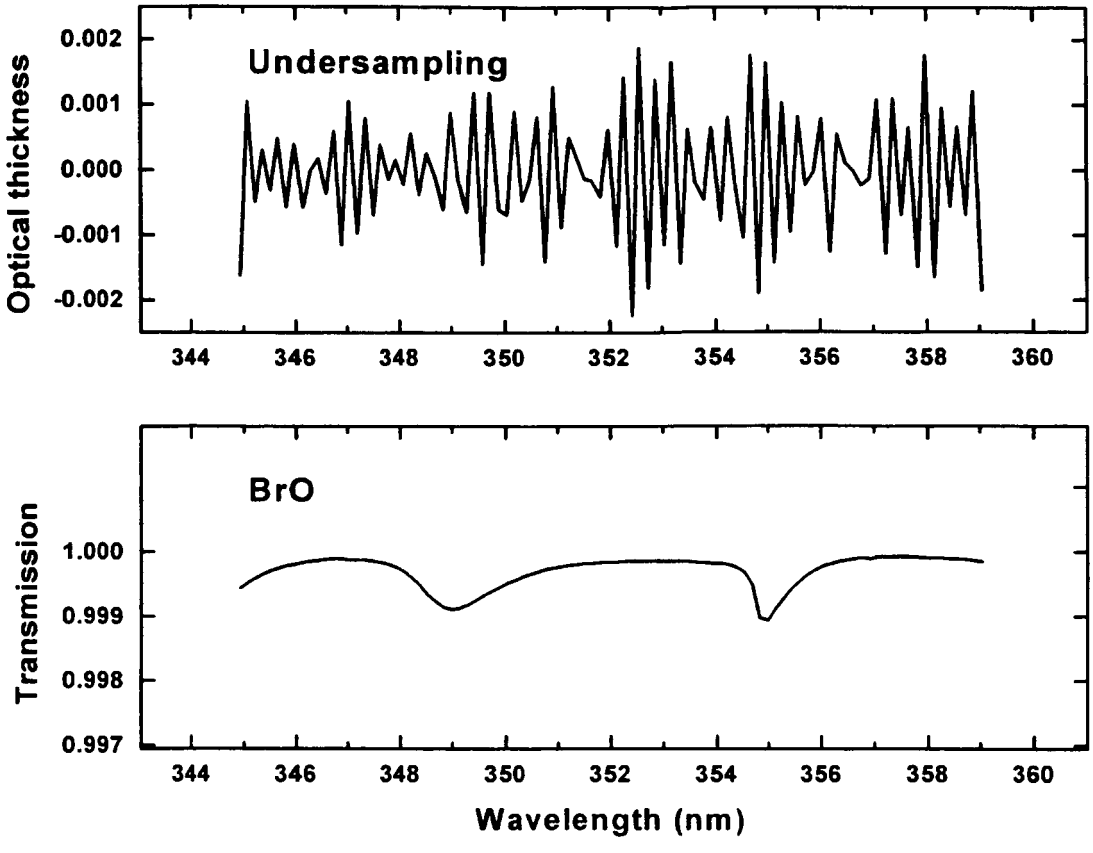
Undersampling
Optical thickness
0.002
0.001
0.000
-0.001
-0.002
344
346
348
350
352
354
356
358
360
BrO
Transmission
1.000
0.999
0.998
0.997
344
346
348
350
352
354
356
358
360
Wavelength (nm)

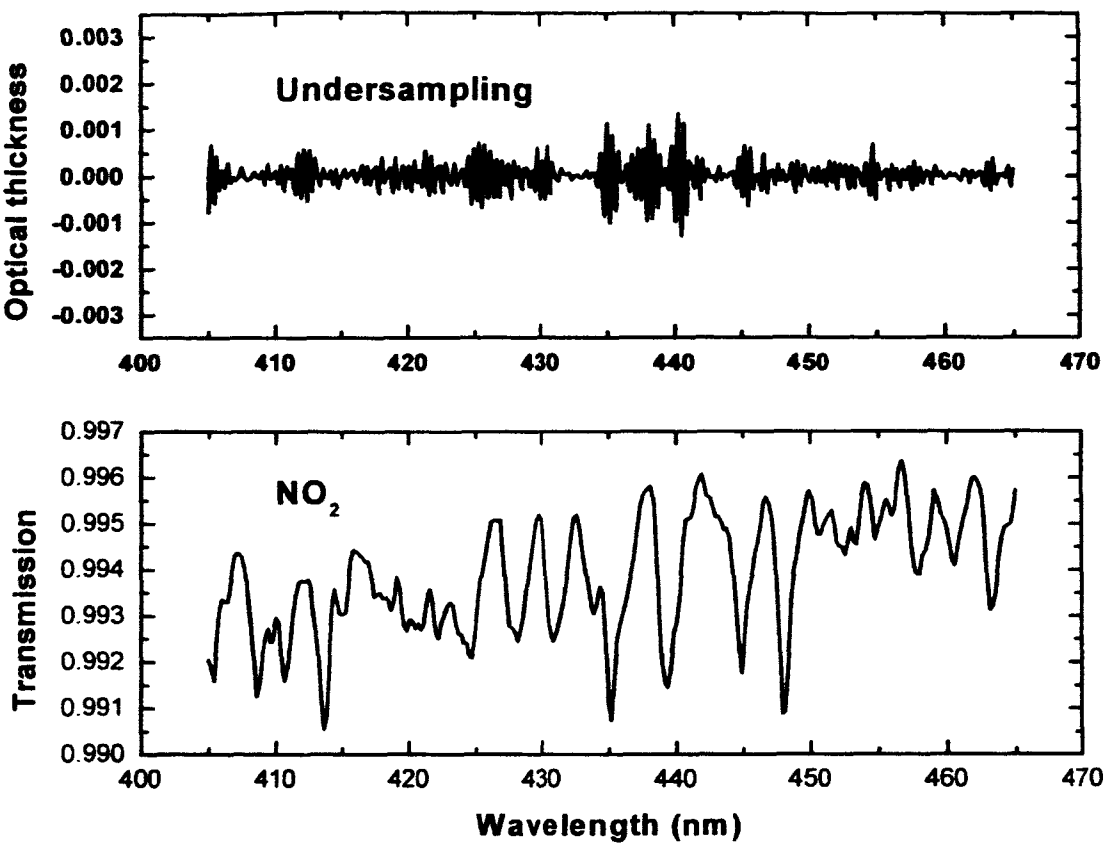
Undersampling
Optical thickness
0.003
0.002
0.001
0.000
-0.001
-0.002
-0.003
400
410
420
430
440
450
460
470
NO2
Transmission
0.997
0.996
0.995
0.994
0.993
0.992
0.991
0.990
Wavelength (nm)

Appendix B

Ozone Profiles and Tropospheric Ozone from Global Ozone Monitoring Experiment

OZONE PROFILES AND TROPOSPHERIC OZONE FROM GLOBAL OZONE MONITORING EXPERIMENT

X. Liu[1], K. Chance[1], C.E. Sioris[1], R.J.D. Spurr[1], T.P. Kurosu[1], R.V. Martin[2], M.J. Newchurch[3], P.K. Bhartia[4]

[1] *Atomic and Molecular Physics Division, Harvard-Smithsonian Center for Astrophysics, 60 Garden Street, Cambridge, MA, USA, Email: xliu@cfa.harvard.edu; kchance@cfa.harvard.edu*
[2] *Department of Physical and Atmospheric Sciences, Dalhousie University, Halifax, NS, Canada*
[3] *Atmospheric Science Department, University of Alabama in Huntsville, Huntsville, Alabama, USA*
[4] *Atmospheric Chemistry and Dynamics Branch, NASA GSFC, Greenbelt, Maryland, USA*

ABSTRACT

Ozone profiles are derived from backscattered radiances in the ultraviolet spectra (290-340 nm) measured by the nadir-viewing Global Ozone Monitoring Experiment using optimal estimation. Tropospheric O_3 is directly retrieved with the tropopause as one of the retrieval levels. To optimize the retrieval and improve the fitting precision needed for tropospheric O_3, we perform extensive wavelength and radiometric calibrations and improve forward model inputs. Retrieved O_3 profiles and tropospheric O_3 agree well with coincident ozonesonde measurements, and the integrated total O_3 agrees very well with Earth Probe TOMS and Dobson/Brewer total O_3. The global distribution of tropospheric O_3 clearly shows the influences of biomass burning, convection, and air pollution, and is generally consistent wiht our current understanding.

1. INTRODUCTION

The retrieval of O_3 profile including the troposphere from Global Ozone Monitoring Experiment (GOME) has been demonstrated in recent years using physics-based approaches [1-4]. These algorithms require very accurate radiometric and wavelength calibrations, and accurate modeling of the atmosphere other than O_3, including clouds, aerosols, and temperature profiles.

This study performs detailed wavelength and radiometric calibrations, improves forward model inputs using our best available knowledge, and derives O_3 profiles and tropospheric O_3 from measured GOME radiances in the ultraviolet. We validate the retrievals against ozonesonde, Dobson/Brewer and TOMS measurements and present the global distribution of tropospheric O_3.

2. DATA AND METHODOLOGY

Ozone profile retrieval from nadir spectra is an ill-conditioned problem. Therefore, we choose the well-known Optimal Estimation (OE) technique for inversion [5]. OE uses available *a priori* knowledge to stabilize retrievals. Because the information content from nadir-viewing spectra is limited, using proper *a priori* climatology is important. We use the TOMS V8 climatology as *a priori* and *a priori* variance. This climatology is month- and latitude-dependent and is derived from Stratospheric Aerosol and Gas Experiment (SAGE), Polar Ozone and Aerosol Measurement (POAM), and ozonesonde observations [6]. A correlation length of 6 km is used to construct the *a priori* covariance matrix.

We improve the wavelength and radiometric calibrations as follows. (1) We derive variable slit widths, and shifts between radiances/irradiances, at every 2-nm region with a high-resolution solar reference spectrum [7]. (2) Shifts between trace gas absorption cross-sections and radiances are fitted in the retrieval. (3) We perform on-line correction of the filling in of solar and telluric absorption features using Ring spectra calculated with a first-order rotational Raman scattering model [8]. Ring spectra are updated when total O_3 changes by $\geq$ 20 Dobson Units (DU). (4) Undersampling of GOME is corrected using a high-resolution solar reference spectrum [9]. (5) We improve the polarization correction to GOME measurements using the GOMECAL package [10] (http://www.knmi.nl/gome_fd/gomecal/).

We improve characterization of the atmosphere with cloud information from the GOME Cloud Retrieval Algorithm [11], monthly mean SAGE II aerosols [12] and GEOS-CHEM tropospheric aerosols [13]; daily European Centre for Medium-Range Weather Forecasts (ECMWF) temperature profiles (http://www.ecmwf.int) for extracting tropospheric O_3 from the temperature-dependent Huggins bands [14], and daily surface pressure from National Centers for Environmental Prediction/National Center for Atmospheric Research (NCEP/NCAR) reanalysis data (http://www.cdc.noaa.gov). Initial albedo is based on derived GOME surface albedo database [15]. Cloud fraction is readjusted from measured reflectance at 370.02 nm where absorption is minimal.

The retrieval uses measurements in the windows 290-307 nm and 327-336 nm. Measurements below 290 nm are not used because of large measurements errors and NO emission

lines. We also find that including band 1b measurements between 307 and 314 nm does not improve the retrievals probably because of inconsistent calibration with band 1a measurements. In addition, GOME slit function and wavelength shifts vary rapidly at the beginning of band 2b (312-327 nm), which makes it difficult to use them to improve the retrievals. The spatial resolution of retrievals is 960 km × 80 km.

Partial columns are typically retrieved on an 11-layer Umkehr-like grid except in the troposphere, where retrieval grids are modified using tropopause pressure and surface pressure. Besides the O_3 variables, the state vector includes an albedo parameter for band 1b, three albedo parameters for band 2b to account for its wavelength-dependence, four cross section shift parameters for each band, four wavelength shift parameters for each band, scaling and shift parameters for minor species (e.g., NO_2, SO_2, BrO), two parameters for undersampling correction, one Ring scaling parameter for band 1a, and three Ring scaling parameters for band 2b to account for multiple scattering, and three parameters to account for the degradation correction in band 1a. The degradation parameters are used only in band 1a because band 1a measurements are more severely degraded. The total O_3 information from band 2b implicitly constrains the degradation correction in band 1a.

We use LIDORT [16] to calculate radiances and weighting functions. The scalar radiances from LIDORT are corrected for neglecting polarization using a look up table.

The retrievals are compared with correlative TOMS V8 and Dobson/Brewer total O_3 measurements and ozonesonde observations. The equator crossing time difference between TOMS and GOME is approximately one hour. We use the gridded TOMS data (1.0° latitude × 1.25° longitude); all TOMS measurements (~ 20 values) within a GOME footprint are averaged. The coincident criteria for Dobson /Brewer and ozonesonde measurements are 1.5° degree in latitude, 600 km in longitude, and 8 hours. Ozonesonde measurements during 1996-2000 at 11 stations are used in these studies (**Table 1**). Six stations also have total O_3 measurements from the Dobson or Brewer measurements.

Table 1. List of ozonesonde stations (abbreviation name), locations, the time period during which data are used, and the availability and type of total O_3 (TOZ) measurements. The measurements at Scoresbysund are obtained from Network for the Detection of Stratospheric Change (NDSC, http://www.ndsc.ncep.noaa.gov). The measurements at Java are obtained from M. Fujiwa before 1998 and from Southern Hemisphere Additional Ozonesondes (SHADOZ) [17] since 1998. Other data are obtained from World Ozone and Ultraviolet Radiation Data Center (WOUDC, http://www.woudc.org/index_e.html).

Station (abbr.)	Location	Time	TOZ
Ny Ålesund (ny)	78.9°N, 11.9°E	96-00	N/A[1]
Scoresbysund (sc)	70.5°N, 22.0°W	96-00	N/A
Sodankylä(so)	67.4°N, 26.7°E	96-98	Brewer
Hohenpeißenberg (ho)	47.9°N, 11.0°E	96-00	Dobson
Hilo (hi)	19.6°N,155°W	96-00	Dobson[2]
Nairobi (nr)	1.3°S, 36.8°E	97-00	Dobson[3]
Java (ja)	7.6°S, 112.7°E	96-00	N/A
Ascension (as)	8.0°S, 14.4°W	97-00	N/A
America Samoa (sa)	14.2°S,170.6°W	96-00	Dobson
Lauder (la)	45.0°S, 169.7°E	96-00	Dobson
Neumayer (ne)	70.7°S, 8.3°W	96-00	N/A

1. Total O_3 is available only during 1996-1997 and is not used.
2. The total O_3 is measured at a close station Mauna Loa (19.5°N, 155.6°E); its surface altitude is 3.4 km.
3. Total O_3 is available only during 1997-1999.

3. RESULTS AND DISCUSSION

3.1. Comparisons with TOMS and Dobson/Brewer Total O_3

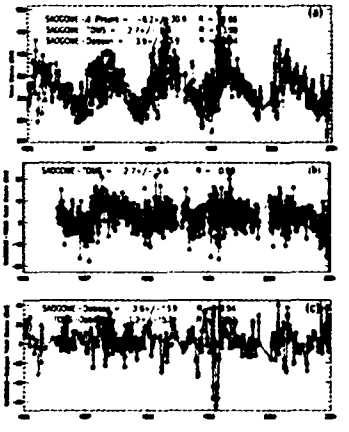

Fig. 1. Comparisons of integrated total O_3 (purple) with TOMS (red) and Dobson total O_3 (green) at Hohenpeißenberg. (a) Total O_3. (b) Difference between GOME and TOMS. (c) Difference between GOME/TOMS and Dobson. The *a priori* O_3 is also shown as yellow in (a).

Fig. 1a shows the time series of integrated total O_3 together with TOMS and Dobson total O_3 at Hohenpeißenberg. Their differences are shown in **Fig. 1b** and **Fig. 1c**. The time series of differences do not change with time, suggesting that band 2 measurements do not degrade much and the severe degradation in band 1a since 1998 [3] are well handled using the above-mentioned degradation correction scheme. We can see that our retrievals agree very well with both TOMS and Dobson total ozone with average biases less than 4 DU. **Table 2** shows the biases, standard deviations, and correlation coefficients between our retrieved, TOMS, and Dobson/Brewer total O_3. The biases are within 7 DU at all stations; the correlation coefficients are greater than 0.92 between GOME and TOMS and greater than 0.87 between GOME and Dobson/Brewer. These biases are within the retrieval uncertainties of different retrievals and the spatiotemporal variability of total O_3. Compared to the *a priori*, we can certainly see significant improvements, with smaller biases and much smaller standard deviations. The standard deviations are

smaller for comparisons with TOMS measurements because of similar spatial domains. In the comparison with Dobson measurements, we are comparing area vs. point measurements; it is expected that the standard deviations will be larger. We note that the standard deviations are larger at higher latitudes because of larger spatiotemporal variability. For example in Fig. 1c, there are a few large differences, greater than 40 DU, between GOME/TOMS retrievals and Dobson measurements in the January and February of 1999. The longitude differences are greater than 5° and the time difference are greater than 4 hours. There are large spatial gradients over this region for these days as seen from TOMS data, suggesting that these large differences result from the large spatiotemporal O_3 variability at mid-latitudes in the winter and early spring.

Table 2. Biases, standard deviations, and correlation coefficients between GOME total O_3 and *A priori*/TOMS/Dobson/Brewer total O_3. The O_3 between retrieval surface to station surface altitude is taken into account in the following comparisons. The units for biases and standard deviations are DU.

Station	GOME-*A Priori*	GOME-TOMS	GOME-Dobson
ny	-23.3±39./0.66	-3.3±8.3/0.99	N/A
sc	-13.3±40/0.68	2.0±6.8/0.99	N/A
so	-29.3±41/0.53	0.0±7.8/0.99	-5.2±14.2/0.97
ho	-6.2±30.6/0.66	2.7±5.5/0.99	3.9±13.9/0.94
hi	-5.1±13.1/0.66	-2.3±4.2/0.97	0.8±6.3/0.95
nr	1.3±12.2/0.22	-1.5±4.8/0.93	-2.9±6.0/0.87
ja	-13.4±7.6/0.62	-5.6±3.8/0.92	N/A/
as	1.8±8.2/0.59	0.2±3.7/0.94	N/A
sa	-9.8±8.3/0.54	-3.9±3.4/0.93	2.3±4.2/0.91
la	-8.5±23.2/0.80	-3.6±6.2/0.99	0.8±18.8/0.88
ne	-26.0±31/0.85	-6.3±7.9/0.99	N/A

3.2. Comparisons of O_3 profiles with ozonesonde

Because ozonesonde measures O_3 only up to ~ 35 km, we can only compare the bottom seven layers. We integrate the ozonesonde profiles to partial columns at each layer corresponding to their collocated GOME retrievals. In order to assess the accuracy of the GOME retrievals, the ozonesonde profiles are not convolved with retrieval averaging kernels because smoothing contributes to retrieval errors. Fig. 2 shows the comparison of retrieved O_3 profiles with ozonesonde measurements at Hohenpeißenberg. We can see that the retrievals agree very well with ozonesonde measurements. The average biases are within 2.5 DU and 10% at each layer (Fig. 3).

Fig. 3 shows the average biases and standard deviations between retrieved/*a priori* profiles and ozonesonde profiles. For Scoresbysund, Sodankylä, Hohenpeißenberg, and Lauder, the comparisons are very good with average biases within 6 DU and 15% at each layer. The standard deviations between retrievals and ozonesonde are usually reduced relative to those between *a priori* and ozonesonde O_3.

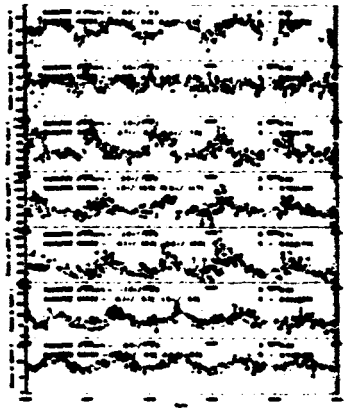

Fig. 2. Comparisons of GOME retrieved (purple circles) and ozonesonde O_3 profiles (green triangles) for the bottom seven layers (0~35 km) at Hohenpeißenberg. The *a priori* are shown as yellow.

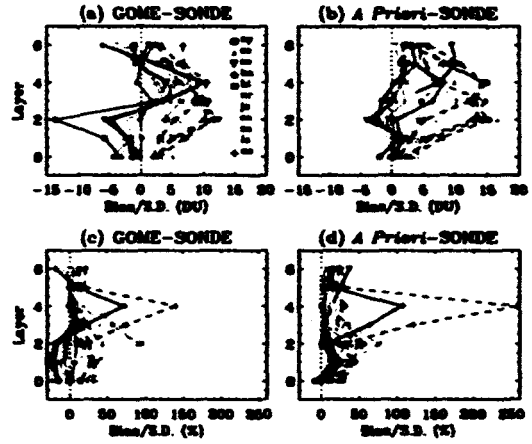

Fig. 3. Mean biases (solid) and standard deviations (dashed) at all stations for (a) GOME – sonde, (b) GOME *a priori* – sonde. (c) and (d) are similar to (a) and (b) except for relative biases and standard deviations.

At Ny Ålesund, there is generally good agreement except at for layer 2 (~10-15 km), where the mean bias is –13 DU, although the difference between *a priori* and ozonesonde is much smaller (-2.6 DU). This difference is usually larger during the spring than the summer, and is slightly correlated with solar zenith angle (R=-0.24) and cloud fraction (R=-0.34). The bias is probably due to the incorrect assignment of ice surface to clouds and is currently under investigation. At Neumayer, large biases occur at layer 4 (~20-25 km) with a mean bias of 10 DU. The relative bias can be greater than 200%, especially when there is strong O_3 depletion and the column O_3 is less than 10 DU. The bias is partly due to similar large bias in the *a priori* O_3. For the five tropical stations, the agreements are within 5 DU and 10% for layers 5 and 6 and are within 4 DU and 30% for layers 0 and 1, but large biases occur at layers 3, 4, and 5. Thompson et al. [17]

also reported large biases between TOMS and SHADOZ integrated and evaluated total O_3. Currently, our integrated total O_3 columns agree very well with Dobson and TOMS total O_3 columns. It is not clear whether these large biases result from retrieval errors or ozonesonde measurement errors. We notice that the biases for those layers at America Samoa and Hilo are actually much smaller before early 1998, when sensor solution for measurements was switched from 1% KI-buffered solution to 2% KI unbuffered solution.

3.3 Comparisons of tropospheric O_3 with ozonesonde

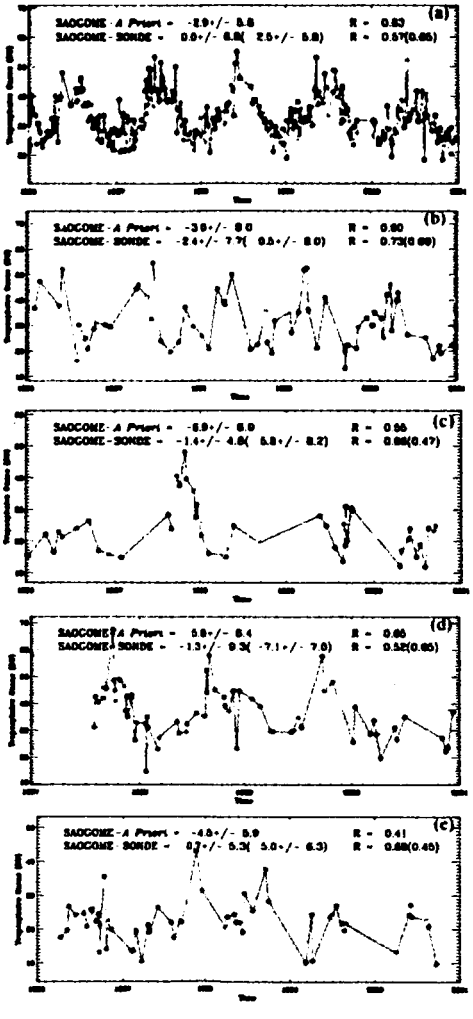

Fig. 4 Comparisons between GOME retrieved (purple circles) and ozonesonde (green triangles) tropospheric O_3 columns at (a) Hohenpeißenberg, (b) Hilo, (c) Java, (d) Ascension, and (e) American Samoa. The *a priori* are also shown as yellow.

Fig. 4 compares the integrated tropospheric O_3 column at five stations. We can see that our retrievals agree very well with ozonesonde measurements. Most of the small-scale variabilities are captured by our retrievals. For example, at Java, although the *a priori* values are usually around 30 DU, our retrievals successfully capture small values (~15 DU) as well as enhanced values (~50 DU) during the period of intense biomass burning resulting from 1997-1998 El Niño event. **Table 3** summarizes the biases, standard deviations and correlation coefficients at all the stations. The average biases are usually within 3 DU and the standard deviations are within 9 DU except at Ny Ålesund, Scoresbysund, and Neumayer, where there are large biases. The large biases at those stations may result from the incorrect treatments of cloud and ice surface. There is a large standard deviation at Ascension Island, which is because the South Atlantic Anomaly can largely affect the retrieval.

Table 3. Biases, standard deviations and correlation coefficients between retrieved/*a priori* and ozonesonde tropospheric O_3. The units for biases and standard deviations are DU.

Station	GOME – SONDE	*A Priori* – SONDE
ny	-7.0±6.0/0.22	0.64±6.5/0.39
sc	-3.5±5.5/0.46	2.6±6.2/0.61
so	-2.0±5.4/0.59	2.7±6.1/0.59
ho	0.0±6.8/0.57	2.4±5.8/0.65
hi	-2.4±7.7/0.73	0.5±8.0/0.68
nr	-3.0±8.0/0.42	-1.8±5.4/0.29
ja	-1.4±4.8/0.86	5.8±8.2/0.47
as	-1.3±9.3/0.52	-7.13±7.0/0.65
sa	0.6±5.3/0.68	5.0±6.3/0.45
la	-1.4±6.4/0.10	-1.0±4.8/0.50
ne	-4.7±6.6/0.78	2.2±4.1/0.92

The retrieval errors in tropospheric O_3 due to random noise and smoothing are less than 3 DU for tropical regions and less than 5 DU for mid-latitude regions. The accuracy in ozonesonde measurements is 5-15% [18]. The natural tropospheric O_3 variability is 20-30% at mid-latitudes [19]; the tropospheric O_3 can change by a factor of 3 at most SHADOZ stations [20]. Considering the spatial and time domain difference and the spatiotemporal variability of tropospheric O_3, we can say that our retrievals are very consistent with ozonesonde measurements within the measurement/retrieval uncertainties and spatiotemporal variability.

3.4 Global distribution of tropospheric O_3

Fig. 5 (top) shows the global distribution of tropospheric O_3 during 2/24-26/1997. In the tropics, there is low O_3 over the Pacific Ocean, where there are intense convection activities. Over North Africa (~0°E, 10°N), a region with intense biomass burning during this period, there is enhanced tropospheric O_3, which is not presented in most of the tropospheric O_3 retrievals [21]. However, the O_3

values are smaller than those over the South Atlantic Ocean, consistent with the observed Atlantic tropospheric paradox [22]. In the Antarctic, the tropospheric O_3 is consistently less than 15 DU. Near 30°N and 30°S, which corresponds to downward motion of Hadley circulation, there are bands of high tropospheric O_3 even over the ocean. These high O_3 values are probably due to the complex interplay of photochemistry and localized/transported pollution under favorable weather conditions. During 9/16-18/1997, the two bands of high O_3 and the low O_3 over Pacific Ocean with shift slightly north with the motion of intertropical convergence zone (ITCZ). There is enhanced tropospheric O_3 over Indonesia, consistent with the intense biomass burning and meteorological conditions (e.g. dry air, less precipitation) caused by the 1997-1998 El Niño event. Over South America, South Africa and the Atlantic Ocean, high O_3 values of 40-60 DU result from intense biomass burning over South Africa and South America.

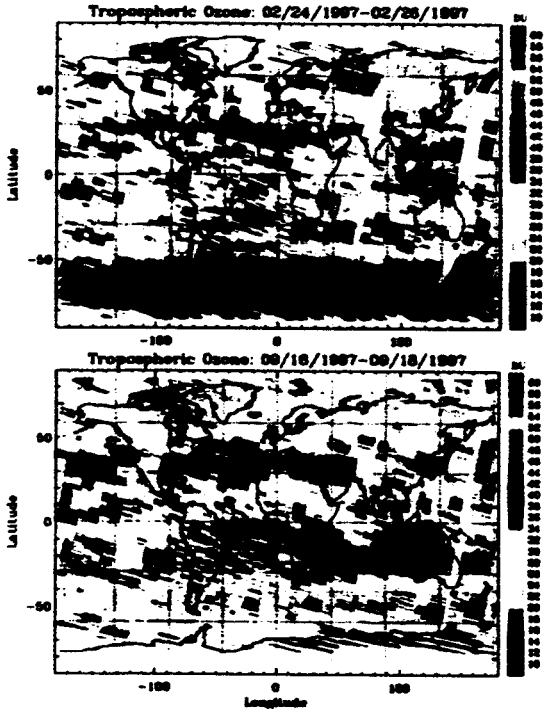

Fig. 5 Three-day composites of global distribution of tropospheric O_3. (a) 2/24-26/1997. (b) 9/16-18/1997. The noisy patterns over the South Atlantic Ocean are caused by the South Atlantic Anomaly.

4. CONCLUSION

An algorithm was developed to retrieve O_3 profiles and tropospheric O_3 from GOME using the optimal estimation technique. We particularly focus on tropospheric O_3 derivation by performing extended wavelength and radiometric calibrations and improving forward model inputs. Tropospheric O_3 is directly retrieved by using tropopause as one of the retrieval layers. We validate our retrievals against TOMS and Dobson/Brewer total O_3 and ozonesonde measurements at 11 high-latitude, mid-latitude, and tropical stations. The integrated total ozone agrees very well with TOMS and Dobson/Brewer measurements with average biases less than 7 DU. Retrieved O_3 profiles generally agree well with ozonesonde measurements except some large biases in the stratosphere at Ny Ålesund, Neumayer, and tropical stations. The large biases at Ny Ålesund and Neumayer may be related to the incorrect assignment of snow/ice surface to clouds. It is unclear whether the large biases at those tropical stations are due to ozonesonde measurement errors or our retrieval errors. The retrieved tropospheric O_3 columns agree very well ozonesonde measurements except at Ny Ålesund and Neumayer, capturing most of low and high O_3 in the ozonesonde measurements. Global distributions of tropospheric O_3 are presented. They clearly shows signals due to biomass burning, convection, air pollution, and transport and are generally consistent with our current knowledge and understanding.

Acknowledgements This study is supported by the NASA Atmospheric Chemistry and Modeling Analysis Program and by the Smithsonian Institution. We thank WOUDC and its data providers, SHADOZ, NDSC, S.B. Anderson and M. Fujiwara for providing ozonesonde measurements. We also thank R. van Oss for providing his software and look-up tables for polarization correction.

References

1. Munro R., et al. Direct measurement of tropospheric ozone from space, *Nature*, 392, 168-171, 1998.
2. Hoogen R., et al. Ozone profiles from GOME satellite data: Algorithm description and first validation, *J. Geophys. Res.*, 104, 8263-8280, 1999.
3. van der A R.J., et al. Ozone profile retrieval from recalibrated GOME data, *J. Geophys. Res.*, 107, 10.1029/2001JD000696 (2002).
4. Hasekamp O.P. and Landgraf J., Ozone profile retrieval from backscattered ultraviolet radiances: The inverse problem solved by regularization, *J. Geophys. Res.*, 106, 8077-8088 (2001).
5. Rodgers C.D., Inverse methods for atmospheric sounding: Theory and practice, ed. 1st. 2000, Singapore: World Scientific Publishing.
6. McPeters R.D., et al. Ozone climatological profiles for Version 8 TOMS and SBUV retrievals, *AGU 2003 Fall meeting*, San Francisco, California, 2003.
7. Chance K.V. and Spurr R.J.D., Ring effect studies: Rayleigh scattering, including molecular parameters for rotational Raman scattering, and the Fraunhofer spectrum, *Appl. Opt.*, 36, 5224-5230, 1997.

8. Sioris C.E. and Evans W.F.J., Impact of rotational Raman scattering in the O_2 *A* band, *Geophys. Res. Lett.*, 27, 4085-4088, 2000.
9. Chance K., Analysis of BrO measurements from the global ozone monitoring experiment, *Geophys. Res. Lett.*, 25, 3335-3338, 1998.
10. Schutgens N.A.J. and Stammes P., A novel approach to the polarization correction of spaceborne spectroscopy, *J. Geophys. Res.*, 108, 4229, doi:10.1029/2002JD002736 (2003).
11. Kurosu T.P., et al. CRAG-Cloud retrieval algorithm for ESA's GOME, *European Symposium on Atmospheric Measurements from Space*, 1999.
12. Bauman J.J., et al. Stratospheric aerosol climatology from SAGE II and CLAES measurements: 2. Results and comparisons, 1984-999, *J. Geophys. Res.*, 108, 4383, doi:10.1029/2002JD002993, 2003.
13. Martin R.V., et al. An improved retrieval of tropospheric nitrogen dioxide from GOME, *J. Geophys. Res.*, 107, 10.1029/2001JD001027, 2002.
14. Chance K.V., et al. Satellite measurements of atmospheric ozone profiles, including tropospheric ozone, from ultraviolet/visible measurements in the nadir geometry: a potential method to retrieve tropospheric ozone, *J. Quant. Spectrosc. Radiat. Transfer*, 57, 467-476, 1997.
15. Koelemeijer R.B.A., et al. A database of spectral surface reflectivity in the range 335-772 nm derived from 5.5 years of GOME observations, *J. Geophys. Res.*, 108, 2003.
16. Spurr R.J.D., et al. A linearized discrete ordinate radiative transfer model for atmospheric remote-sensing retrieval, *J. Quant. Spectrosc. Radiat. Transfer*, 68, 689-735, 2001.
17. Thompson A.M., et al. "Southern Hemisphere Additional Ozonesondes (SHADOZ) 1998-2000 tropical ozone climatology 1. Comparison with Total Ozone Mapping Spectrometer (TOMS) and ground-based measurements, *J. Geophys. Res.*, 108, 8238, doi:10.1029/2001JD000967, 2003.
18. Logan J.A., An analysis of ozonesonde data for the troposphere: Recommendations for testing 3-D models and development of a gridded climatology for tropospheric ozone, *J. Geophys. Res.*, 104, 16,115-16,149, 1999.
19. WMO, Scientific Assessment of Ozone Depletion: 1998. NASA, NOAA, UNEP, WMO, EC: Geneva, Switzerland. pp.1-44, 1999.
20. Thompson A.M., et al. Southern Hemisphere Additional Ozonesondes (SHADOZ) 1998-2000 tropical ozone climatology 2. Tropospheric variability and the zonal wave-one, *J. Geophy. Res.*, 108, 8241, doi:10.1029/2002JD002241, 2003.
21. Newchurch M.J., et al. Critical Assessment of TOMS-derived Tropospheric Ozone: Comparisons with Other Measurements and Model Evaluation of Controlling Processes. *Eos. Trans. AGU*, 82 (20), Spring Meet. Suppl. Abstract A52A-09, 2001.
22. Thompson A.M., et al. A Tropical Atlantic Paradox: Shipboard and Satellite Views of a Tropospheric Ozone Maximum and Wave-one in January-February 1999, *Geophys. Res. Lett.*, 27, 3317-3320, 2000.